

A spiral galaxy’s mass distribution uncovered through lensing and dynamics

Wilma H. Trick^{1*}, Glenn van de Ven¹ and Aaron A. Dutton¹

¹*Max-Planck-Institute for Astronomy, Königstuhl 17, 69117 Heidelberg, Germany*

Accepted ???. Received ???; in original form ???

ABSTRACT

We analyse the stellar and dark matter distribution in the spiral galaxy SDSS J1331+3638 (J1331) by means of two independent methods: gravitational lensing and dynamical Jeans modelling. Hubble Space Telescope (HST) imaging by Treu et al. (2011) reveals, that J1331’s bulge is superimposed by a quadruplet of extended lensing images. By fitting a gravitational potential model to the image positions, we constrain the mass inside the Einstein radius ($R_{\text{ein}} = 0.91 \pm 0.02$ arcsec) to within 4% ($M_{\text{ein}} = (7.8 \pm 0.3) \cdot 10^{10} M_{\odot}$). From Multi-Gaussian Expansions (MGE) of J1331’s surface brightness distribution we find that J1331 has a total luminosity of $L_{I,\text{tot}} \simeq 5.6 \cdot 10^{10} L_{I,\odot}$ and an effective radius of $R_{\text{eff}} \simeq 2.6$ arcsec = 5.6 kpc. [TO DO: apparent brightness is boring, right?]

According to the long-slit major axis stellar kinematics from Dutton et al. (2013), J1331 has a counter-rotating stellar core inside ~ 2 arcsec. We model the observed stellar kinematics in J1331’s central regions by finding MGE models for the stellar and dark matter distribution that solve the axisymmetric Jeans equations. We find that J1331 requires a steep total mass-to-light ratio gradient in the center to reproduce the observed stellar kinematics. The best fit dynamical model predicts a total mass inside the Einstein radius consistent with the lens model, and vice versa the lens model gives an successful prediction for the observed kinematics in the galaxy center. For a dynamical model including a NFW dark matter halo, we constrain the halo to have virial velocity $v_{200} \simeq 240 \pm 40$ km/s and a concentration of $c_{200} \simeq 8 \pm 2$ in case of a moderate tangential velocity anisotropy of $\beta_z \simeq 0.4 \pm 0.1$. The NFW halo models can successfully reproduce the signatures of J1331’s counter-rotating stellar core and predict J1331’s rotation curve at larger radii. However, all these models were more massive than expected from the gas rotation curve at larger radii, and failed to reproduce the steep drop in measured velocity dispersion at [TO DO: WHAT RADIUS???]. This could indicate a non-trivial re-distribution of matter due a possible minor merger event in J1331’s past.

Key words: blabla – blabla: bla.

1 INTRODUCTION

[TO DO]

Dark matter general

- The flat rotation curves of galaxies were the first indication, that galaxies could reside in large and massive, more or less spherical halos made of invisible dark matter \rightarrow stellar movements in solar neighbourhood (Oort 1932), $H\alpha$ rotation curves of external galaxies (Rubin et al. 1978)
- Standard model of cosmology, based on the by the

Planck Mission, predicts $\sim 32\%$ of the universes content is in the form of matter and $\sim 85\%$ of the total matter is non-baryonic dark matter.

Lensing to measure mass

- Completely independent method to measure mass of galaxies is gravitational lensing
- massive galaxies can act as gravitational lenses, deflect light of background sources, gives rise to multiple images
- By 2010 over 200 strong gravitational galaxy lenses had been discovered (Treu 2010) and the number is still rising
- On galaxy scales strong gravitational lensing is sensitive

* E-mail: trick@mpia.de

to the total projected matter amount inside approximately ~ 1 arcsec.

Dynamical modelling to measure mass

- Gas rotation curves are useful to measure matter distribution at large radii
- gas on circular orbits \rightarrow directly circular velocity curve and mass profile.
- But: gas has dissipative nature, concentrated to mid-plane \rightarrow sensitive to disturbances by e.g. bars, spiral arms
- stars are dissipationless, present almost everywhere in the galaxy \rightarrow very good tracers of the underlying gravitational potential \rightarrow but much more complex motions: bulk rotation around principal axis, plus random motion components in all coordinate directions \rightarrow velocity anisotropy \rightarrow degeneracy with matter distribution
- modelling: account for stellar rotation, dispersion and velocity anisotropy
- e.g. solution of the Jeans equations for an assumed velocity anisotropy, e.g. Cappellari (2008)
- dynamical modelling of stellar kinematics also at smaller radii \rightarrow complement lensing investigation of the matter distribution in the center of galaxies
- Other modelling methods: Schwarzschild's orbital superposition approach (van den Bosch et al. 2008)

Dark Matter Halos

- Cosmological cold dark matter N-body simulations suggest that dark matter halos take a cuspy shape, following a NFW profile (Navarro et al. 1996)
- central dark matter density cusps are not observed in dark matter dominated galaxies (dwarfs); if they exist in more massive galaxies depends strongly on stellar mass-to-light ratio. Overall, observations suggest cored dark matter halos \rightarrow core-cusp problem, might be due to a yet unknown interaction between dark matter and baryons

SWELLS Survey

TO DO

- Sloan WFC Edge-on Late-type Lens Survey (SWELLS) WFC = Wide field camera (Treu et al. 2011; Dutton et al. 2011; Brewer et al. 2012; Barnabè et al. 2012; Dutton et al. 2013; Brewer et al. 2014)
- Treu et al. (2011) give measurements for the apparent AB magnitudes for the HST/WFPC2 I-band/F814W filter for disk and bulge, as well as stellar masses for stellar population models for a Chabrier [TO DO: REF] and Salpeter [TO DO: REF] initial mass function (IMF).
- dedicated to find spiral galaxy strong lenses, to combine lensing and dynamical modelling to break degeneracies inherent in both methods.
- picked galaxies in SDSS whose spectra had to different redshifts within 3 arcsec, which makes it likely to capture strong lenses with typical Einstein radii of 1 arcsec. Sufficiently inclined galaxies were picked by eye. Follow up high resolution imaging with the Hubble Space Telescope's (HST) Wide-Field Planetary Camera 2 (WFPC2) was performed (Treu et al. 2011)).

Characteristics of J1331

- SDSS J1331+3638 (J1331)
- approximate hubble type Sb, Spiral galaxy almost edge-on
- first discovered by Sloan digital sky survey (SDSS) [TO DO: REF]
- Treu et al. (2011) identified it as a strong lens
- Its coordinates on the sky are right ascension = 202.91800° and a declination = 36.46999° (epoch J2000).
- This galaxy is at a redshift of $z_d = 0.113$ (Brewer et al. (2012)).
- large reddish bulge and bluish spiral arms, see Fig. 1a and 1b
- superimposed by quadruplet of extended bluish images at a redshift of $z_s \simeq 0.254$ [TO DO: REF], see Fig. 1c, approximately at a distance of 1 arcsec from the galaxy center (which is a typical Einstein radius).
- Lens image redshift $z_s = 0.254$ (Brewer et al. 2012)
- lensed object might be a star-forming blob of a background galaxy.
- Lensing properties first analysed by Brewer et al. (2012)
- rather edge-on \rightarrow possible to measure rotation curves. Dutton et al. (2013) measured the gas and stellar rotation curves along the major axis. Fitted galaxy model to gas kinematics at large radii, and lensing result
- large counter-rotating core, see Fig. 1d
- possible minor merger in the past
- background object: possibly bright star forming region in the spiral arms of background galaxy

Goal of this work

- constraining the matter distribution in a galaxy, disentangling stellar and dark matter component at smaller radii
- using two independent methods, lensing and dynamics
- testing, if Jeans modelling works also in the presence of counter-rotating cores
- focus on the smaller radii, as Dutton et al. (2013) was focusing on outer regions
- complementing the work by [SWELLS paper on lensing and lensing/dynamcis TO DO: find] by an in depth analysis
- ideal case: investigating how a minor merger modifies the mass distribution of a galaxy

Data used

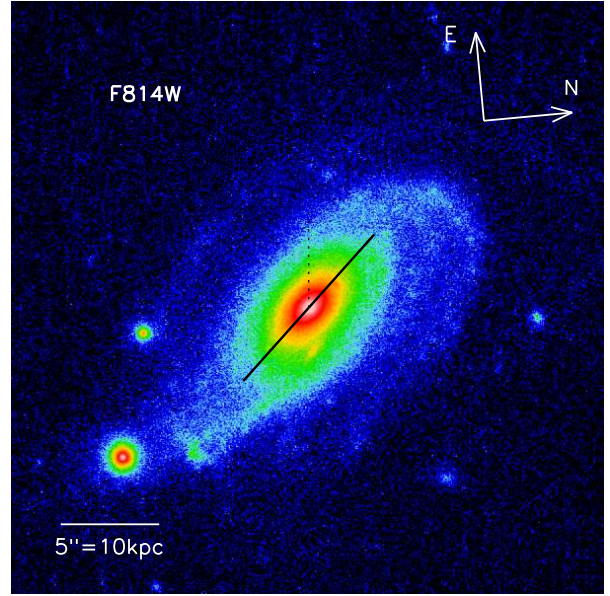
- Hubble Space Telescope (HST)/WFPC2/WFC3 imaging by Treu et al. (2011), see Fig. 1a and 1b
- Dutton et al. (2013) measured the gas and stellar rotation curves along the major axis. see Fig. 1b and 1d

Methods

- similar analysis of J1331 as van de Ven et al. (2010) has done with the Einstein cross
- lensing: fitting scale-free galaxy model to image positions (Evans & Witt 2003)
- photometry: MGE expansion of surface brightness in the F814W filter (deconvolution with PSF), apparent magnitude, total luminosity, effective radius
- Jeans modelling: jeans axisymmetric modelling (JAM) by Cappellari (2008) to fit model predictions for the second velocity moments to the stellar kinematics data



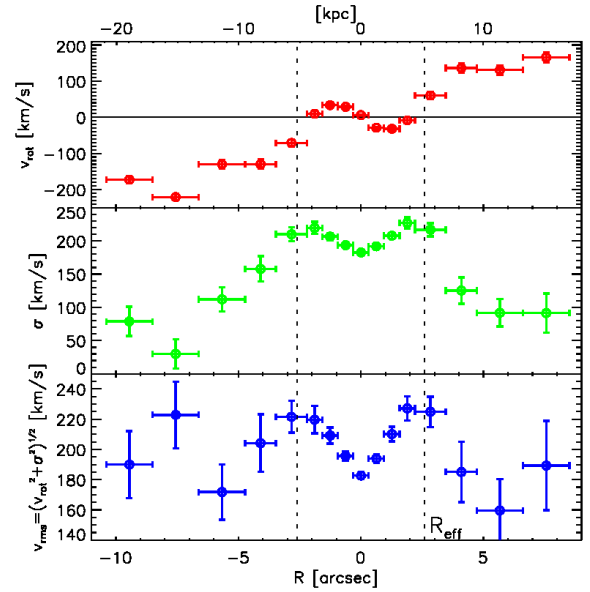
(a) J1331 in F450W ("blue")



(b) J1331 in F814W ("red")



(c) The lensing images



(d) Stellar Kinematics by Dutton et al. (2013)

Figure 1. Hubble Space telescope (HST) images and stellar kinematics of the galaxy SDSS J1331+3638 (J1331), which has a large counter-rotating core and whose bulge acts as a strong lens for a bluish background source. *Panel (a) and (b):* HST/WFPC2/WFC3 images of J1331 by Treu et al. (2011) in two filters, F450W in panel (a) and F814W in panel (b). The galaxy's coordinates on the sky are right ascension $\alpha = 202.91800^\circ$ and declination $\delta = 36.46999^\circ$ (epoch J2000). Image orientation and scaling are indicated in panel (a); the scaling transformation from arcseconds to the physical size of the galaxy in kpc uses the galaxy's redshift $z_d = 0.113$ (Brewer et al. 2012) (i.e. assumes an angular diameter distance of 414 Mpc). The color scaling of these two images is the same. The black solid line in panel (b) shows the orientation of the major-axis. The line has a length of 10 arcsec and indicates the region within which we carry out the Jeans modelling. [TO DO: NOT ALL THE TIME.??????] *Panel (c):* The central region of J1331 in F450W, surface brightness subtracted. An IRAF ellipse ??? fit to the F450W surface brightness in panel (a) was subtracted from the image. The (smoothed) residuals within the white square in panel (a) are shown in panel (c). Four bright blobs (A,B,C and D) become visible, which are arranged in a typical strong lensing configuration around the center of the galaxy (G). *Panel (d):* Stellar Kinematics along the galaxy's major axis as measured by Dutton et al. (2013), line-of-sight rotation velocity v_{rot} , line-of-sight velocity dispersion σ and the rms-velocity $v_{\text{rms}} = \sqrt{v_{\text{rot}}^2 + \sigma^2}$. The dotted line in panel (b) indicates the galaxy's effective half-light radius (in the F814W filter), $R_{\text{eff}} = 2.6'' = 5.2$ kpc. The v_{rot} curve reveals that J1331 is counter-rotating within R_{eff} . [TO DO: Add (x,y) axis in figure b).??????]

[TO DO]

2 MODELLING

2.1 Multi-Gaussian Expansion Formalism

Multi-Gaussian Expansions (MGE) are used to parametrize the observed surface brightness or projected total mass of a galaxy as a sum of N two-dimensional, elliptical Gaussians (Bendinelli 1991; Monnet et al. 1992; Emsellem et al. 1994, 1999). This work makes use of the algorithm and code¹ by Cappellari (2002). We assume all Gaussians to have the same center and position angle ϕ , i.e. orientation of w.r.t. the y' -axis of the coordinate system with polar coordinates (R', θ') [TO DO: CHECK]. Then the surface brightness can be written as

$$I(R', \theta') = \sum_{i=1}^N I_{0,i} \exp \left[-\frac{1}{2\sigma_i^2} \left(x'^2 + \frac{y'^2}{q_i^2} \right) \right] \quad (1)$$

$$\text{with } I_{0,i} = \frac{L_i}{2\pi\sigma_i^2 q_i^2} \quad (2)$$

$$\text{and } x'_i = R' \cos(\theta' - \phi)$$

$$y'_i = R' \sin(\theta' - \phi),$$

where $I_{0,i}$ is the central surface brightness of each Gaussian, L_i its total luminosity, σ_i its dispersion along the major axis and q_i the axis ratio between the elliptical Gaussians major and minor axis.

We can also expand the telescopes point-spread function (PSF) as a sum of circular Gaussians,

$$\text{PSF}(x, y) = \sum_j \frac{G_j}{2\pi\delta_j^2} \exp \left[-\frac{1}{2\delta_j^2} (x^2 + y^2) \right], \quad (3)$$

where $\sum_j G_j = 1$ and δ_j are in this case the dispersions of the circular PSF Gaussians. In this case the observed surface brightness distribution is a convolution of the intrinsic surface brightness in Eq. (1) with the PSF in Eq. (3): $(I * \text{PSF})(x', y')$ is then again a sum of Gaussians and can be directly fitted to an image of the galaxy in question.

$I(R', \theta')$ describes the intrinsic, to 2D projected light distribution or surface density of the galaxy. Under the assumption that the galaxy is oblate and axisymmetric, and given the inclination angle i of the galaxy with respect to the observer, MGEs allow an analytic deprojection of the 2D MGE to get a 3D light distribution or density $\nu(R, z)$ for the galaxy,

$$\nu(R, z) = \sum_i \nu_{0,i} \exp \left[-\frac{1}{2\sigma_i} \left(R^2 + \frac{z^2}{q_i^2} \right) \right]. \quad (4)$$

The flattening of each axisymmetric 3D Gaussian q_i and its central density $\nu_{0,i}$ follow from the observed 2D axis ratio

q'_i and surface density $I_{0,i}$ as

$$q_i^2 = \frac{q'^2_i - \cos^2 i}{\sin^2 i}$$

$$\nu_{0,i} = \frac{q'_i I_{0,i}}{q_i \sqrt{2\pi\sigma_i^2}}.$$

2.2 Strong Gravitational Lensing Formalism and Lens Model

Lensing Formalism. A gravitational lens is a mass distribution, whose gravitational potential Φ acts as a lens for light coming from a source positioned somewhere on a plane behind the lens. The angular diameter distance from the observer to the lens is D_d , to the source plane it is D_s and the distance between the lens and source plane is D_{ds} . The deflection potential of the lens is its potential, projected along the line of sight z and rescaled to

$$\psi(\vec{\theta}) := \frac{D_{ds}}{D_d D_s} \frac{2}{c^2} \int \Phi(\vec{r} = D_d \vec{\theta}, z) dz, \quad (5)$$

where $\vec{\theta}$ is a 2-dimensional vector on the plane of the sky. The light from the source at $\vec{\beta} = (\xi, \eta)^2$ is deflected according to the lens equation

$$\vec{\beta} = \vec{\theta} - \vec{\nabla}_{\theta} \psi(\vec{\theta}) \Big|_{\vec{\theta}_i} \quad (6)$$

into an image $\vec{\theta}_i = (x_i, y_i)$. The gradient of the deflection potential $\vec{\nabla}_{\theta} \psi(\vec{\theta})$ is equal to the angle by which the light is deflected multiplied by D_{ds}/D_s .

The total time delay of an deflected light path through $\vec{\theta}$ with respect to the unperturbed light path is given by

$$\Delta t(\vec{\theta}) = \frac{(1+z_d)}{c} \frac{D_d D_s}{D_{ds}} \left[\frac{1}{2} (\vec{\theta} - \vec{\beta})^2 - \psi(\vec{\theta}) \right], \quad (7)$$

(Narayan & Bartelmann 1999). According to Fermat's principle the image positions will be observed at the extrema of $\Delta t(\vec{\theta})$.

The inverse magnification tensor

$$\mathcal{M}^{-1} \equiv \frac{\partial \vec{\beta}}{\partial \vec{\theta}} \stackrel{(6)}{=} \left(\delta_{ij} - \frac{\partial^2 \psi}{\partial \theta_i \partial \theta_j} \right) \quad (8)$$

describes how the source position changes with image position. It also describes the distortion of the image shape for an extended source and its magnification due to lensing according to

$$\mu \equiv \frac{\text{image area}}{\text{source area}} = \det \mathcal{M}.$$

Lines in the image plane for which the magnification becomes infinite, i.e. $\det \mathcal{M}^{-1} = 0$, are called *critical curves*. The corresponding lines in the source plane are called *caustics*. The position of the source with respect to the caustic determines the number of images and their configuration and shape with respect to each other.

The *Einstein mass* M_{ein} and *Einstein radius* R_{ein} are defined via the relation

$$M_{\text{ein}} \equiv M_{\text{proj}}(< R_{\text{ein}}) \stackrel{!}{=} \pi \Sigma_{\text{crit}} R_{\text{ein}}^2,$$

² ξ and η are cartesian coordinates on the plane of the sky.

¹ Michele Cappellari's IDL code package for fitting MGEs to images is available online at <http://www-astro.physics.ox.ac.uk/~mxc/software>. The version from June 2012 was used in this work.

where $\Sigma_{\text{crit}} \equiv \frac{c^2}{4\pi G} \frac{D_s}{D_d D_{ds}}$ is the critical density and $M_{\text{proj}}(< R_{\text{ein}})$ is the mass projected along the line-of-sight within R_{ein} . M_{ein} is similar to the projected mass within the critical curve M_{crit} .

Lens Model. Following Evans & Witt (2003) we assume a scale-free model

$$\psi(R', \theta) = R'^\alpha F(\theta) \quad (9)$$

for the lensing potential, consisting of an angular part $F(\theta)$ and a power-law radial part, with (R', θ) being polar coordinates on the plane of the sky. The case $\alpha = 1$ corresponds to a flat rotation curve. We expand $F(\theta)$ into a Fourier series,

$$F(\theta) = \frac{a_0}{2} + \sum_{k=1}^{\infty} (a_k \cos(k\theta) + b_k \sin(k\theta)). \quad (10)$$

For this scale-free lens model the lens equation (6) becomes

$$\begin{pmatrix} \xi \\ \eta \end{pmatrix} = \begin{pmatrix} R'_i \cos \theta_i - R'_i{}^{\alpha-1} (\alpha \cos \theta_i F(\theta_i) - \sin \theta_i F'(\theta_i)) \\ R'_i \sin \theta_i - R'_i{}^{\alpha-1} (\alpha \sin \theta_i F(\theta_i) + \cos \theta_i F'(\theta_i)) \end{pmatrix} \quad (11)$$

(Evans & Witt 2003), where $F'(\theta) = \partial F(\theta)/\partial \theta$. When we fix the slope α , then the lens equation is a purely linear problem and can be solved numerically for the source position (ξ, η) and the Fourier parameters (a_k, b_k) given one observed image at position $(x_i = R'_i \cos \theta_i, y_i = R'_i \sin \theta_i)$.

Model fitting. As described above our lensing model has the following free parameters: the source position (ξ, η) , and the radial slope α and Fourier parameters (a_k, b_k) of the lens mass distribution in eq. (9) and (10). We want to find the lensing model which minimizes for all four images the distance between the observed image positions $\vec{\theta}_{oi}$ and those predicted by the lensing model $\vec{\theta}_{pi}$. Because we want to avoid solving the lens equation (cf. eq. (6) and (11)) for θ_{pi} , we follow Kochanek (1991) and cast the calculation back to the source plane using the magnification tensor in eq. (8) to approximate $\vec{\theta} \simeq (\partial \vec{\theta}/\partial \vec{\beta}) \vec{\beta} = \mathcal{M} \vec{\beta}$ and the χ^2_{lens} that the fit wants to minimize becomes

$$\begin{aligned} \chi^2_{\text{lens}} &= \sum_{i=1}^4 \left| \begin{pmatrix} \frac{1}{\Delta_x} & 0 \\ 0 & \frac{1}{\Delta_y} \end{pmatrix} (\vec{\theta}_{pi} - \vec{\theta}_{oi}) \right|^2 \\ &\simeq \sum_{i=1}^4 \left| \begin{pmatrix} \frac{1}{\Delta_x} & 0 \\ 0 & \frac{1}{\Delta_y} \end{pmatrix} \mathcal{M}|_{\vec{\theta}=\vec{\theta}_{oi}} \begin{pmatrix} \xi - \tilde{\xi}_i \\ \eta - \tilde{\eta}_i \end{pmatrix} \right|^2, \end{aligned}$$

where (Δ_x, Δ_y) are the measurement errors of the image positions $\vec{\theta}_{oi}$. $\mathcal{M}|_{\vec{\theta}=\vec{\theta}_{oi}}$ is the magnification tensor and $(\tilde{\xi}_i, \tilde{\eta}_i)$ the source position according to the lens equation, both evaluated at $\vec{\theta}_{oi}$. Following van de Ven et al. (2010) we add a term

$$\chi^2_{\text{shape}} = \lambda \sum_{k \geq 3} \frac{(a_k^2 + b_k^2)}{a_0^2}$$

which forces the shape of the mass distribution to be close to an ellipse. The total χ^2 to minimize is therefore

$$\chi^2 = \chi^2_{\text{lens}} + \chi^2_{\text{shape}}$$

We set $a_1 = b_1 = 0$, which corresponds to the choice of origin; in this case the center of the galaxy.

To be able to constrain the slope α , we would have needed

flux ratios for the images as in van de Ven et al. (2010). But the extended quality of the images, possible dust obscuration and surface brightness fluctuations due to microlensing events, as well as the uncertainty in surface brightness subtraction make flux determination too unreliable and we do not include them in the fitting.

[TO DO: eq. to Equation, fig. to Figure, §to Section, vec to vect, cf to see, tab. to Table]

2.3 Jeans Axisymmetric Modelling (JAM)

Jeans axisymmetric models (JAM) assume galaxies (a) to be collisionless, i.e. the collisionless Boltzmann equation for the distribution function $f(\vec{x}, \vec{v}, t)$ has to be satisfied ($\frac{df(\vec{x}, \vec{v}, t)}{dt} = 0$), (b) in a steady state ($\frac{\partial}{\partial t} = 0$), (c) axisymmetric (best described in cylindrical coordinates (R, z, ϕ) and $\frac{\partial}{\partial \phi} = 0$). From this follow the axisymmetric Jeans equations as the vector-valued first moment of the Boltzmann equation, i.e.

$$\int \frac{df}{dt} d^3v = 0.$$

To be able to solve the Jeans equations, additional assumptions about the velocity ellipsoid tensor $\langle v_i v_j \rangle$ have to be made. We follow Cappellari (2008) and assume firstly, that the galaxy's velocity ellipsoid is aligned with the cylindrical coordinate system, i.e. $\langle v_i v_j \rangle = 0$ for $i \neq j$. Secondly, we assume a constant ratio between the radial and vertical 2nd velocity moments,

$$\beta_z \equiv 1 - \langle v_z^2 \rangle / \langle v_R^2 \rangle. \quad (12)$$

This reduces the Jeans equations to two equations for $\langle v_z^2 \rangle$ and $\langle v_\phi^2 \rangle$, that can be solved by means of one integration,

$$n \langle v_z^2 \rangle (R, z) = \int_0^\infty n \frac{\partial \Phi}{\partial z} dz \quad (13)$$

$$n \langle v_\phi^2 \rangle (R, z) = R \frac{\partial}{\partial R} \left(\frac{n \langle v_z^2 \rangle}{1 - \beta_z} \right) + \frac{n \langle v_z^2 \rangle}{1 - \beta_z} + R n \frac{\partial \Phi}{\partial R}, \quad (14)$$

where $n(\vec{x}) = \int f(\vec{x}, \vec{v}) d^3v$ is the number density of tracers and $\Phi(\vec{x})$ the galaxy's gravitational potential, generated by the mass density $\rho(\vec{x})$ via Poisson's equation.

The JAM modelling approach by Cappellari (2008) makes use of expressing the tracer density and the mass density as MGEs (see also Emsellem et al. (1994)). The density of stellar tracers is assumed to be proportional to the observed and deprojected brightness distribution $\nu(R, z)$ in Eq. (4). The mass density $\rho(R, z)$ consists of several sets of MGEs: One MGE, that is usually taken to be $\nu(R, z)$ multiplied by a constant stellar mass-to-light ratio Υ_* , describes the distribution of stellar mass in the galaxy. (To mimic gradients of mass-to-light ratio, each Gaussian could be assigned its own $\Upsilon_{*,i}$.) To add a Navarro-Frenck-White (NFW) (Navarro et al. 1995, 1996) dark matter halo component, a MGE generated from a fit to a NFW profile can be added to the stellar component. [TO DO: Maybe remove detailed description of the mass MGE here, if it is described in detail somewhere else.] The gravitational potential is generated from the mass MGE by integrating the Poisson equation (Emsellem et al. 1994). Equations 13 and 14 together with 12 provide the velocity dispersion tensor $\langle v_i v_j \rangle = \langle v_i^2 \rangle$ (with $i, j \in \{R, \phi, z\}$). It is then rotated by the inclination angle i to the coordinate system of the observer $((x', y')$

being the plane of the sky and z' the line-of-sight, where x' is aligned with the galaxy's major axis). Taking a light-weighted projection along the line-of-sight gives a model prediction for the line-of-sight velocity second moment, which is comparable to actual spectroscopic measurements of the second velocity moment. Details of the derivation using the MGE formalism are given in Cappellari (2008) and repeated in van de Ven et al. (2010), we therefore just quote the result by Cappellari (2008) (their Equation 28) for the line-of-sight second velocity moment prediction from the Jeans equations,

$$(I\langle v_{\text{los}}^2 \rangle)(x', y') \quad (15)$$

$$= 4\pi^{3/2} G \int_0^1 \sum_{k=1}^N \sum_{j=1}^M \nu_{0,k} q_j \rho_{0,j} u^2 \times \frac{\sigma_k^2 q_k^2 \left(\cos^2 i + \frac{\sin^2 i}{1-\beta_{z,k}} \right) + \mathcal{D} x'^2 \sin^2 i}{(1-\mathcal{C}u^2) \sqrt{(\mathcal{A} + \mathcal{B} \cos^2 i) [1 - (1-q_j^2)u^2]}} \quad (16)$$

$$\times \exp \left\{ -\mathcal{A} \left[x'^2 + \frac{(\mathcal{A} + \mathcal{B}) y'^2}{\mathcal{A} + \mathcal{B} \cos^2 i} \right] \right\} du, \quad (17)$$

$$(18)$$

with N Gaussians describing the tracer distribution and M Gaussians describing the mass distribution, $\rho_{0,j}$ being the j -th mass density Gaussian evaluated at ($R=0, z=0$) and

$$\mathcal{A} = \frac{1}{2} \left(\frac{u^2}{\sigma_j^2} + \frac{1}{\sigma_k^2} \right)$$

$$\mathcal{B} = \frac{1}{2} \left\{ \frac{1-q_k^2}{\sigma_k^2 q_k^2} + \frac{(1-q_j^2)u^4}{\sigma_j^2 [1 - (1-q_j^2)u^2]} \right\}$$

$$\mathcal{C} = 1 - q_j^2 - \frac{\sigma_k^2 q_k^2}{\sigma_j^2}$$

$$\mathcal{D} = 1 - \frac{q_k^2}{1-\beta_{z,k}} - \left[\left(1 - \frac{1}{1-\beta_{k,z}} \right) \mathcal{C} + \frac{1-q_j^2}{1-\beta_{z,k}} \right] u^2.$$

The JAM modelling code by Cappellari (2008) evaluates numerically Equation 16 for a given luminous tracer and mass distribution MGE and a given inclination.

[TO DO: make primed and unprimed coordinate systems clear.]

Data comparison. As data we use stellar line-of-sight rotation velocities $v_{\text{rot}} \equiv \langle v_{\text{los}} \rangle$ [TO DO: consistent, los or rot] and velocity dispersions σ as described in §3. The JAM models give us a prediction for the second line-of-sight velocity moment v_{los} . The root mean square (rms) line-of-sight velocity v_{rms} allows a data-model comparison by relating theses velocities according to

$$v_{\text{rms}}^2 = \langle v_{\text{los}}^2 \rangle = v_{\text{rot}}^2 + \sigma^2.$$

The model in Eq. [TO DO] predicts the intrinsic $\langle v_{\text{los}}^2 \rangle$ at a given position on the sky, which have then to be modified to model the mode of observation, to be comparable to the measurements. The measured v_{rms} is a light-weighted mean for a pixel along the long-slit of the spectrograph, with height $L_y = 1$ arcsec (Dutton et al. 2013) and a certain given extent in along the major axis, L_x , i.e. for a rectangu-

lar aperture

$$\text{AP}(x, y) = \begin{cases} 1 & \text{for } -\frac{L_x}{2} \leq x \leq +\frac{L_x}{2} \text{ and } -\frac{L_y}{2} \leq y \leq +\frac{L_y}{2} \\ 0 & \text{otherwise} \end{cases}.$$

The light arriving at the spectrograph itself was subject to seeing, i.e. a Gaussian

$$\text{PSF}(x, y) = \mathcal{N}(0, FWHM/2\sqrt{2\ln 2})$$

with $FWHM=1.1$ arcsec (Dutton et al. 2013). The model predictions have therefore to be convolved with the convolution kernel

$$\begin{aligned} K(x, y) &= (\text{PSF} * \text{AP})(x, y) \\ &= \frac{1}{4} \prod_{u \in \{x, y\}} \left[\text{erf} \left(\frac{L_u/2 - u}{\sqrt{2}\sigma_{\text{seeing}}} \right) + \text{erf} \left(\frac{L_u/2 + u}{\sqrt{2}\sigma_{\text{seeing}}} \right) \right] \end{aligned}$$

and weighted by the surface brightness $I(x, y)$ [TO DO: primed x and y or not????]

$$I_{\text{obs}} = I * K$$

$$\langle v_{\text{los}}^2 \rangle_{\text{obs}} = \frac{(I\langle v_{\text{los}}^2 \rangle) * K}{I_{\text{obs}}}.$$

If provided with the convolution kernel, the JAM code by Cappellari (2008) [TO DO: reference code] performs the convolution numerically. We set $L_x = 0.21$ arcsec as the width of the model pixel, and get a prediction for the actual measurements in bins of width 0.63, 1.26 and 1.89 arcsec (Dutton et al. 2013) as light-weighted mean from each 3, 6 and 9 model pixels.

Rotation curve. The intrinsic rotation curve is the first velocity moment $\langle v_\phi \rangle = \sqrt{\langle v_\phi^2 \rangle - \sigma_\phi^2}$. The observed rotation curve is the projection of the light-weighted contributions to $\langle v_\phi \rangle$ along the line-of-sight (Cappellari (2008)),

$$I\langle v_{\text{los}} \rangle = \int_{-\infty}^{+\infty} \nu \langle v_\phi \rangle \cos \phi \sin i \, dz'.$$

The first velocity moments cannot be uniquely determined from the Jeans equations, which give only a prediction for the second velocity moments. Further assumptions are needed to separate the second velocity moments into ordered and random motion. Cappellari (2008) assumes that in a steady state there is no streaming velocity in R direction, i.e. $\langle v_R \rangle = 0$ and therefore $\sigma_R^2 = \langle v_R^2 \rangle$. Then Cappellari (2008) relates the dispersions in R and ϕ direction such that

$$\langle v_\phi \rangle = \sqrt{\langle v_\phi^2 \rangle - \sigma_\phi^2} \equiv \kappa \sqrt{\langle v_\phi^2 \rangle - \langle v_R^2 \rangle},$$

and the κ parameter quantifies the rotation: $\kappa = 0$ means no rotation at all and $|\kappa| = 1$ describes a velocity dispersion ellipsoid that is a circle in the R - ϕ plane (Cappellari 2008). The sign of κ determines the rotation direction. We can assign a constant κ_k to every Gaussian in the MGE formalism and

$$\nu \langle v_\phi \rangle = \left[\nu \sum_k \kappa_k^2 (\langle v_\phi^2 \rangle_k - \langle v_R^2 \rangle_k) \right]^{1/2}$$

is then the light-weighted circular velocity curve, given the second velocity moments found from the Jeans equations. To model the counter-rotating core of J1331 with one free parameter for, we employ the condition that the overall $\kappa(R)$ profile should smoothly and relatively steeply transition

from $\kappa(R) = -\kappa' < 0$ at small R [TO DO: Check, ich glaube das hier ist das intrinsische R in Zylinder-Coordinaten] trough $\kappa(R_0) \equiv 0$ and increase to $\kappa(R) = \kappa' > 0$ at large R . Our imposed profile is

$$\kappa(R) = \kappa' \frac{R^2 - R_0^2}{R^2 + R_0^2}. \quad (19)$$

We find κ' by matching the model $\langle v_{\text{los}} \rangle$ with the symmetrized v_{rot} data, where for a given κ' the κ_k are found from fitting the MGE generated profile $\kappa(R) = \sum_k \kappa_k \nu_k(r) / \sum_k \nu_k(r)$ to Eq. (19). The observed zero point is at $R'_0 \approx 2$ arcsec. In the deprojected galactic plane the radius of zero rotation would be at a $R_0 \gtrsim 2$ arcsec, and we choose it to be at 2.2 arcsec.

3 DATA

For our lensing and dynamics analysis of J1331 we use on the one hand Hubble Space Telescope (HST) imaging by Treu et al. (2011) in two filters (F450W and F814W), and on the other hand line-of-sight stellar kinematics along J1331's major axis by Dutton et al. (2013).

Redshift. [TO DO: WHO???] found from SDSS spectra that J1331 has two redshifts inside 1 arcsec: The smaller one, $z_d = 0.113$, is the redshift of J1331 itself, the larger one, $z_s = 0.254$, is the redshift of the lensed background source (Brewer et al. 2012). According to its redshift and the WMAP5 [TO DO: CHECK] cosmology (Dunkley et al. 2009), J1331 has an angular diameter distance of 414 Mpc, which translates into a transverse scaling of 1 arcsec $\hat{=}$ 2.01 kpc.

HST imaging. We use the follow-up HST imaging, with which Treu et al. (2011) confirmed that J1331 is indeed a strong gravitational lens [TO DO: REALLY???]. They performed high resolution imaging with the Hubble Space Telescope's (HST) Wide-Field Planetary Camera 2 (WFPC2) and its WF3 CCD chip. The images we are using are a combination of four exposures with each an exposure of 400s and were drizzled to a pixel scale of 1 pixel = 0.05 arcsec. In particular we use the images in the filters F450W, to identify the positions of the bluish lensing images, and F814W to create a surface brightness MGE model of the reddish bulge (I-band), used in the JAM dynamical modelling.

Stellar kinematics. For the dynamical modelling we also use the stellar kinematics for J1331 measured by Dutton et al. (2013). They obtained long-slit spectra along J1331's major-axis with the Low Resolution Imaging Spectrograph (LRIS) on the Keck I 10m telescope. The width of the slot was 1 arcsec and the seeing Conditions had a FWHM of ~ 1.1 arcsec. Spectra for spatial bins of different widths along the major axis were extracted. Analogously to Dutton et al. (2011) they measured line-of-sight rotation velocities (v_{rot}) and stellar velocity dispersion (σ) by fitting Gaussian line profiles to emission lines in these spectra. Gas kinematics were extracted from fits to H α and NII lines, as tracers for ionized gas.

The stellar kinematics, v_{rot} , σ and $v_{\text{rms}}^2 = v_{\text{rot}}^2 + \sigma^2$ are shown in Figure 1d. The rotation curve reveals a

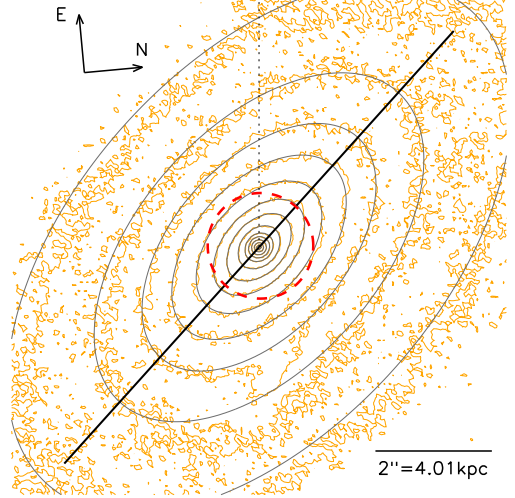


Figure 2. MGE for J1331's inner regions: Comparison of contours with constant F814W surface brightness of J1331's central region (orange lines) with the corresponding iso-brightness contours of the best fit MGE in table 2, convolved with the PSF in table 2, (gray lines). The MGE model is a good representation of the galaxy's light distribution within ~ 5 arcsec. Image scaling and orientation are indicated in the figure. The black line has a length of 10 arcsec and its orientation corresponds to the galaxy's position angle as found in table 3. For comparison the Einstein radius as found in table ??? is indicated as red dashed line. This MGE is used in the dynamical Jeans modelling in §???. [TO DO: explain how this MGE is used in dynamical modelling]

counter-rotating core within 2 arcsec $\simeq 4$ kpc. Outside of ~ 3.5 arcsec there is a steep drop in the dispersion, which is expected at the boundary between the pressure supported bulge and the rotationally supported disk, which appears around this radius in the F450W filter in Figure 1a. However, in the brighter F814W filter in Figure 1b the large reddish bulge extends out to ~ 5 arcsec.

Inside of ~ 4 arcsec, the data appears to be symmetric, outside of this the assumption of axisymmetry seems not to be valid anymore, considering the data. We add -2.3 km/s to the v_{rot} to ensure $v_{\text{rot}}(R=0) \sim 0$ as a possible correction term for a systematic misjudgement of the systemic velocity. We also symmetrize the data within 4 arcsec and assign a minimum error of $\delta v_{\text{rms}} > 5$ km/s to the v_{rms} data. In the JAM modelling, which is based on the assumption of axisymmetry, only kinematics within ~ 2.5 and 4 arcsec are used. Another reason to restrict to modelling on the bulge region is that our MGE in Table 2 is only a good representation of J1331's F814W light distribution inside ~ 5 arcsec.

[TO DO: How to deal with the typo in J1331s name???

4 RESULTS

4.1 Surface Photometry for J1331 with MGEs

In §??? we derived a mass model for J1331 from Lensing. In this section set up a model for the galaxy's intrinsic light distribution in terms of an MGE, which we will then compare to the mass distribution. The light model will also be

Table 2. J1331’s F814W MGE: Parameters of the best fit MGE to the F814W surface brightness of J1331 in Fig. 1b. The fit is best inside an radius of 5 arcsec. The galaxy center and position angle, which gives the orientation of the MGE with respect to the original image, are given in table 3. This MGE is used in the dynamical modelling in §???. The first column gives the total F814W luminosity of the Gaussian in Eq. (2) in units of counts. The second column is the corresponding I-band peak surface brightness in Eq. (1) in units of a luminosity surface density, calculated from the first column following the procedure described in §???. The third and fourth column give the dispersion and the last column the axis ratio of the Gaussian in Eq. (1).

k	total luminosity L_k [counts]	surface density $I_{0,k}$ [L_\odot/pc^2]	Gaussian dispersion		axis ratio
			σ_k [arcsec]	σ_k [kpc]	q'_k
1	9425.96	20768.	0.051	0.103	1.00
2	13173.0	3161.2	0.178	0.358	0.76
3	40235.0	1588.2	0.503	1.008	0.58
4	67755.2	502.25	1.180	2.368	0.56
5	203677.	136.51	3.891	7.805	0.57

Table 3. Galaxy Parameters of J1331

redshift	z_d	0.113	(Brewer et al. 2012)
angular diameter distance	D_d [Mpc]	414	
scaling	1 kpc / 1 arcsec	2.006	
position angle	ϕ [degrees]	wrt what???	
average axis ratio	q'	0.598	
average ellipticity	$\epsilon = 1 - q'$	0.402	
apparent I-band magnitude	m_I [mag]	15.77	
total I-band luminosity	$L_{\text{tot},I}$ [$10^{10} L_\odot$]	5.6	
effective half-light radius	R_{eff} [arcsec]	2.6	
	R_{eff} [pc]	5.2	

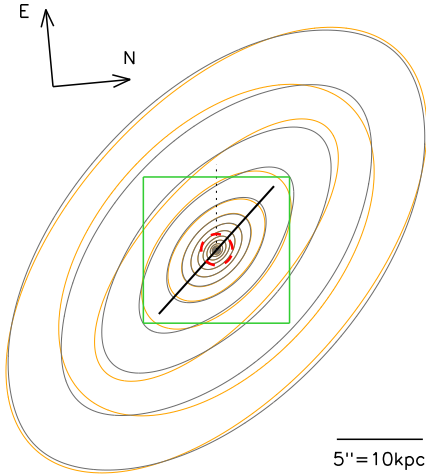


Figure 3. MGE for J1331’s outer regions: Comparison of contours with constant surface brightness of the smooth IRAF ELIPSE model for J1331 in the F814W filter (yellow) with a corresponding best fit MGE (gray lines). The green box corresponds to the image section shown in Fig. 2, with the Einstein radius as dashed red line. [TO DO: caption]

the basis of the dynamical Jeans modelling in §???

To derive J1331’s surface brightness distribution, we use the HST image in the infrared F814W filter, shown in Fig. 1b. In infrared J1331’s central old and smooth stellar component is more extended than in the F450W filter in Fig. 1a, which is more sensitive to young clumpy star-forming regions. In infrared the bulge is also much brighter than the

Table 1. F814W PSF MGE: Parameters of the circular four-Gaussian MGE in Eq. (3 fitted to the radial profile of the synthetic HST/F814W PSF image by [TO DO].

k	G_k	δ_k [arcsec]
1	0.184	0.038
2	0.485	0.085
3	0.222	0.169
4	0.109	0.487

bluish lens images and the imaging is less prone to extinction. The F814W image is therefore best suited for fitting a MGE.

PSF for the HST/F814W filter. We find a radial profile for the HST/F814W filter PSF from circular annuli within a synthetic PSF image from [TO DO: Where did we get this image from???], ignoring diffraction spikes. The one-dimensional MGE fit of Eq. (3) to this radial profile is performed using the code by [TO DO: REF and footnote to code]. The MGE parameters of the normalized PSF model are given in Tab. 1.

MGE for the inner regions. We fit a MGE to the smooth central region within radius ~ 5 arcsec of the HST/WFPC2/WF3/F814W image of J1331 in Fig. 1b. Bright objects close to the galaxy, blobs possibly belonging to the background galaxy and parts of the foreground spiral arm were masked during the fit. J1331’s galaxy center, position angle and average apparent ellipticity (see table 3) are found from the images weighted first and second moment.

The MGE fit, as performed by the code Cappellari (2002), splits the image in annuli with the given ellipticity and position angle and sectors of 5° width and fits an 5-Gaussian MGE of the form in Eq. (1) convolved with the PSF MGE in table 1 to it. The best fit MGE (PSF convolved) is compared to the data in Fig. 2 and the corresponding parameters of the intrinsic surface brightness distribution are given in table 2. The fit is a very good representation of the light distribution in the inner 5 arcsec, but underestimates the light distribution outside of this.

MGE for the outer regions. To get an handle on the light distribution also in the outer parts of J1331, where spiral arms dominate, we first fit a IRAF ELLIPSE [TO DO: How to reference??] model to the F814W image (masking the brightest blobs in the spiral arms and outer regions). Only then we fit a 7-Gaussian MGE to the smooth ellipse model. The MGE does not perfectly reproduce the flatness of the ellipse model at every radius, but considering the spiral arm dominated outer regions of J1331, it is good enough for an approximate handling of the overall light distribution.

Transformation into physical units. To transform the MGE in units of counts into physical units, we apply a simplified version of the procedure described in Holtzman et al. (1995), analogous to [TO DO: Cappellari Read me file?]. The scaling of the drizzled HST/WFC3 images is $S = 0.05$ arcsec/pixel and the total exposure time $T = 1600$ sec. The total F814W luminosity in counts of each Gaussian of the MGE has a central surface brightness in counts per pixel of

$$C_0[\text{counts/pixel}] = \frac{L[\text{counts}]}{2\pi\sigma[\text{pixel}]^2q}.$$

This is then transformed into an I-band surface brightness via

$$\mu_I \simeq -2.5 \log_{10} \left(\frac{C_0[\text{counts/pixel}]}{T[\text{sec}] \cdot S[\text{arcsec/pixel}]^2} \right) + Z + C + A_I, \quad (20)$$

where $Z \simeq 21.62$ is a the zero-point from Holtzman et al. (1995) (updated according to Dolphin (2000, 2008)) for the photometric system of the HST/WFPC2 camera and the F814W filter plus a correction for the difference in gain between calibration and observation. $C = 0.1$ corrects for the finite aperture of the WFPC2. And $A_I = 0.015$ mag is the extinction in the I-band towards J1331, according to the NASA/IPAC Extragalactic Database [TO DO: proper reference]. The color-dependent correction between the F814W filter and the I-band of the UBVRI photometric system is small (Holtzman et al. 1995) and we neglect it therefore. The last step is to transform the surface brightness μ_i in mag to the I-band surface density of the Gaussian in L_\odot/pc^2 as

$$I_0[L_\odot\text{pc}^{-2}] = (64800/\pi)^2 (1+z)^4 10^{0.4(M_{\odot,I}-\mu_I)},$$

where the term with z accounts for redshift dimming and $M_{\odot,I} = 4.08$ mag is the sun's absolute I-band magnitude (Binney & Merrifield 1998). The luminosity $L_k[\text{counts}]$ and the corresponding surface brightness density $I \equiv I_{0,k}[L_\odot\text{pc}^{-2}]$ of each Gaussian are given in Table 2. [TO DO: I'm really confused about this. Check, that everything is correct and the naming of quantities, e.g. with or with-

out subscripts of 0, is fine??] [TO DO: Maybe shift to appendix??]

Inclination. To estimate the inclination of J1331 with respect to the observer, we use the observed axis ratio of the flattest ellipse in the IRAF Ellipse [TO DO] model for J1331, which is $q' = 0.42$. This is similar to the disk axis ratio of $q' = 0.40$ found by Treu et al. (2011) [TO DO: CHECK]. If a typical thickness of an oblate disk was around $q_0 \sim 0.2$ [TO DO: REF: Holmberg 1985], the inclination would follow from $\cos^2 i = \frac{q'^2 - q_0^2}{1 - q_0^2}$ and a correction of $+3^\circ$ [TO DO: REF: Tully 1988]. Our estimate for the inclination is therefore $i \approx 70^\circ$.

Total luminosity and effective radius. J1331's total I-band luminosity is easily determined by summing up the luminosity contributions of all the Gaussians of the MGE for the outer regions (shown as gray lines in Fig. 3). We find $L_{\text{tot},I} \simeq 5.6 \cdot 10^{10} L_\odot$. This corresponds to an apparent magnitude of $m_I = 15.77$ mag. We determine the circularized effective radius R_{eff} of J1331 from the definition $L(< R_{\text{eff}}) \equiv \frac{1}{2} L_{\text{tot}}$ and the growth curve $L(< R)$ from the MGE model of the outer regions [TO DO: Maybe I need a table anyway??], where R is the projected radius on the sky [TO DO: Or is it R' ??]. We find the effective radius to be $R_{\text{eff}} \simeq 2.6 \text{ arcsec} \hat{=} 5.2 \text{ kpc}$. All values are summarized in Table 3.

[TO DO: Stuff to mention]

- the deprojecten if the galaxy under the assumption of oblate axisymmetry and an estimated inclination of $\sim 70^\circ$ can be performed analytically.

4.2 Mass distribution from Lensing

Image Positions. We determine the positions of the lensing images by first subtracting a smooth model for the galaxy's surface brightness from the original image. As models we use MGE fits and IRAF ellipse fits (see Sections 2.1 and 4.1) to the galaxy in each the F450W and F814W filter. (For example the MGE we use for F814W is the MGE given in Table 2 convolved with the PSF in Table 1.) The lensing images become then visible in the residuals (see Figure 1c), in which we smooth out noise smaller than the PSF. Because the lensing images are extended, we use the position of the brightest pixel in each of the images. We also use the F450W-MGE subtracted residuals from Brewer et al. (2012). The lensing positions as determined from the latter are given in Table 4. The scatter of lensing positions as determined from subtracting different surface brightness models from the galaxy in different filters gives an error of ± 1 pixel on the image positions. We find slightly different positions for the peak of the surface brightness in the different filters and apply correspondingly an error of one diagonal pixel to the brightness peak in the F450W image which we use as center of the galaxy.

Eight image position coordinates allow us to fit a lens mass model with only < 8 free parameters. We therefore do not fit Fourier components (a_k, b_k) with $k > 3$.

Even though the constraints from the image positions on α

	A	B	C	D	G
x_i [pixel]	12.1	-8.5	21.7	-3.3	$0.5 \pm \sqrt{2}$
y_i [pixel]	16.6	-10.4	-0.5	19.2	$0.5 \pm \sqrt{2}$

Table 4. Positions of the lensing images (A-D) and the galaxy center (G) in Figure 1c. The image positions were determined from the lens subtracted image for J1331 in Figure 4 of Brewer et al. (2012), rotated to the (x, y) coordinate system in Figure 1c. The pixel scale is 1 pixel = 0.05 arcsec and the error of each image position is ± 1 pixel. *SMALL PROBLEM: Somehow I used $\sqrt{2}$ pixel as the error on the galaxy center in the Monte Carlo sampling code instead of the 0.5 pixel I claim here. Should I change this table and the error bars in the figures to match this bug???*

is very weak, we were however able to show that the image positions in Table 4 are consistent with a model with flat rotation curve. In the following we therefore set $\alpha = 1$.

Best fit lens model. The best fit lens model for the image positions in Table 4 is given in the first column of Table 5. Figure 4a shows the corresponding critical curve, caustic and Einstein radius, and the best fit source position. In this case, where $\alpha = 1$, the critical curve is also an equidensity contour of the galaxy model (Evans & Witt 2003), which appears to have an elliptical mass distribution. This critical curve is called *tangential*, because of the tangential orientation of the images close to it. The source is located close to a cusp of the diamond-shaped caustic: a lensing configuration for which we indeed expect four images. This is a good indication that indeed all four images are indeed lensing images of the same object. Figure 4b overplots the smoothed residuals from the F450W image subtracted by the IRAF ellipse fit to the surface brightness with the contours of the best fit model’s time delay surface. This demonstrates that, although we did not include any information about the shape of the lensing images in the fit, it is consistent with the predicted distortion for an extended source by the best fit lens model.

To estimate how the uncertainties in the determination of the image positions and galaxy center affect the results, we Monte Carlo sample random positions from a two-dimensional Normal distribution centered at the positions in Table 4 and a standard deviation corresponding to the measurement error. A Gaussian fit to the resulting distributions of best fit values leads to the constraints on the shape parameters and Einstein quantities in the second column in Table 5. We therefore constrain the Einstein radius to within 2%, $R_{\text{ein}} = (0.91 \pm 0.02)$ arcsec and the projected mass within the critical curve with a relative error of 4%, $M_{\text{crit}} = (7.9 \pm 0.3) \cdot 10^{10} M_{\odot}$. Our measurement of R_{ein} is consistent with that from Brewer et al. (2012), $R_{\text{ein,SWELLS}} = (0.96 \pm 0.04)$ arcsec (which used a singular isothermal ellipsoid as lens mass model and the intermediate-axis convention of the critical curve as the Einstein radius). The relative difference between our critical mass and that of Brewer et al. (2012), $M_{\text{crit,SWELLS}} = (8.86 \pm 0.61) \cdot 10^{10} M_{\odot}$, is 13%.

Comparison with Light Distribution. The surface mass distribution as predicted by the best fit model in Ta-

ble 5 is shown in Figure 5b. We introduced random noise according to the uncertainties in the Fourier shape parameters to create a mock observation that visualizes the effect of the measurement errors. From the mock image’s second moment we find an average axis ratio for the lens mass model of $q_{\text{lens}} \simeq 0.695$, which is consistent with the one found by Brewer et al. (2012), $q_{\text{lens,SWELLSIII}} = 0.67 \pm 0.09$, while the light’s average axis ratio in Table 3 is $q' = 0.598$.

To estimate the total mass-to-light ratio within the Einstein radius $\Upsilon_{\text{I,tot}}^{\text{ein}} = M_{\text{ein}}/L_{\text{I,ein}}$, we first integrate the MGE in Table 2 to get the total luminosity within the Einstein radius $L_{\text{I,ein}}$. $L_{\text{I,ein}}$ and $\Upsilon_{\text{I,tot}}^{\text{ein}}$ are given in Table 6. $\Upsilon_{\text{I,tot}}^{\text{ein}} \sim 5.6$ is consistent or slightly larger than the stellar mass-to-light ratio assuming a Salpeter Initial Mass Function $\Upsilon_{\text{I,*}}^{\text{Salpeter}} = 4.7 \pm 1.2$ according to Treu et al. (2011) and Table 8 (see also discussion in Section 5.1). We use $\Upsilon_{\text{I,tot}}^{\text{ein}}$ to transform the observed surface brightness in the F814W filter into a surface mass density to compare it to the lensing mass distribution (Figure 5a). Figure 5c then compares equidensity contours at the same values of both the predicted lens mass distribution and the observed surface brightness times $\Upsilon_{\text{I,tot}}^{\text{ein}}$.

Figure 5 leads to the following three findings: (1) The mass predicted from lensing and the observed light distribution are oriented in the same direction (i.e. have the same position angle). (2) Within and around the Einstein radius, mass and light distribution have a similar elliptical shape, while further out the mass distribution is slightly rounder. (3) The light distribution drops faster than the mass with increasing radius. Astrophysical reasons for the differences in observed light and measured mass distribution could be, e.g. an apparent change of shape due to dust extinction, a strongly changing $\Upsilon_{\text{I,*}}$, or the stellar component of the galaxy could be superimposed by a more roundish dark matter component. We have to note however that the mass distribution is only constraint around the Einstein radius and otherwise an extrapolation.

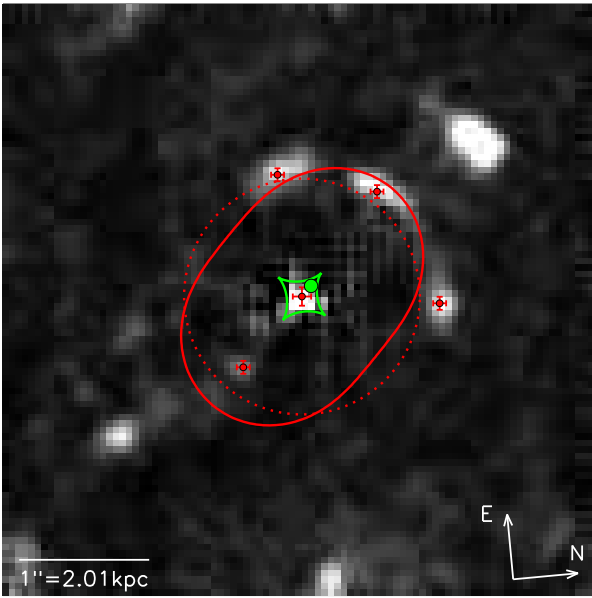
4.3 JAM based on Surface Brightness

... with the Lens Mass Model. Our first JAM model uses the mass distribution which we found from lensing constraints in §4.2 to generate an independent prediction for the v_{rms} curve following the procedure in §2.3. In addition to the flat rotation curve model with $\alpha = 1$ in Table 5, we also investigate a lens model, which was found as a best fit to the lensing images when assuming a [TO DO: rising or droppint???] rotation curve slope of $\alpha = 1.1$. The predictions are compared with the data in Figure 6. The agreement between the lensing prediction and the observed kinematics within $R' \sim 3$ arcsec is striking, especially around the Einstein radius. The $\alpha = 1$ model fits the wings nicely, while the $\alpha = 1.1$ model recreates almost exactly the observed central dip. The sharp drop in v_{rms} around $R' \sim 3$ arcsec [TO DO: make sure all projected Rs are R'] cannot be reproduced, however. But outside of the Einstein radius our lensing models are only extrapolations and the true constraint is around the Einstein radius.

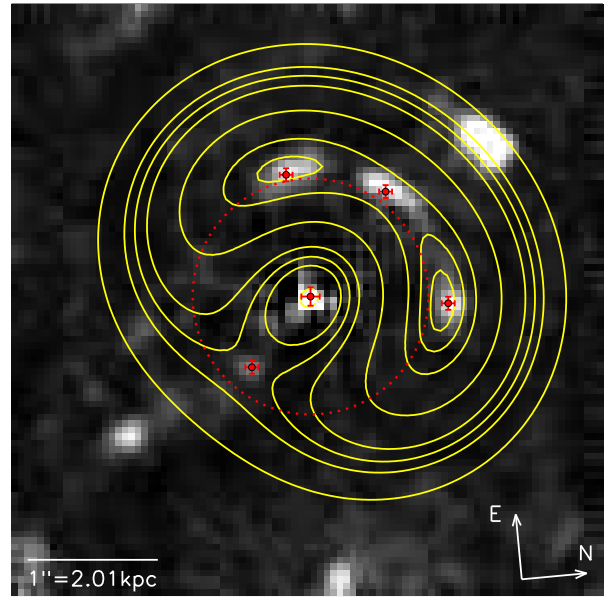
... with “Mass-follows-Light” and Velocity Anisotropy. Our second JAM model is a mass-follows-light model, which are often used in dynamical JAM

Table 5. [TO DO: Caption] ??? in Table 4, for $\alpha = 1$

		lens model for peak image positions		lens model from Monte Carlo sampling of image positions	
Einstein radius	R_{ein} [arcsec]	0.907	0.91	\pm 0.02	(2%)
Einstein mass	M_{ein} [$10^{10} M_{\odot}$]	7.72	7.8	\pm 0.3	(4%)
Critical mass	M_{crit} [$10^{10} M_{\odot}$]	7.87	7.9	\pm 0.3	(4%)
Source position	ξ [arcsec]	0.095	0.09	\pm 0.03	(28%)
	η [arcsec]	0.107	0.10	\pm 0.03	(27%)
Fourier coefficients	a_0	1.814	1.82	\pm 0.04	(2%)
	a_2	0.012	0.011	\pm 0.004	(35%)
	b_2	-0.057	-0.06	\pm 0.01	(25%)
	a_3	-0.0001	0.0000	\pm 0.0006	
	b_3	-0.0002	0.000	\pm 0.001	



(a) Best fit critical curve, Einstein radius, caustic, source position.



(b) Time delay surface.

Figure 4. Best fit lens model in Table 5 found from the image positions. In the background we show the central region of J1331 in the F450W filter, subtracted by an Irf Ellipse model of the F450W surface brightness and smoothed by boxcar smoothing of the order of the PSF size. The four bluish lensing images are clearly visible and we mark the brightness peaks in Table 4 as well as the galaxy center (G) as red dots. The Einstein radius of the best fit lens model is shown as a red dotted circle. *Panel (a)* Besides the image positions and Einstein radius, the critical curve (red solid line) is shown in the lens plane. The caustic (green solid line) corresponding to the critical curve and best fit source position (green dot), which are both located in the source plane, are shown as well. For $\alpha = 1$ (which we assumed for our lens model) the critical curve is a contour of constant surface density of the mass model. *Panel (b)* The yellow lines show (arbitrary) contours of the time delay surface given by Equation 7 of the best fit lens model. Not only the position of the extrema, but also their shape is consistent with the observed, extended images, even though we did not use information about the image shape in the analysis. The other two right blobs (north east of A, south east of B) might be star forming regions of the background galaxy as well. [TO DO: Add A, B, C, D in the figure to make clear which image is which.]

Table 6. Total I-band (F814W) luminosity inside the Einstein radius R_{ein} , found from integrating the MGE in Table 2 and corresponding total mass-to-light ratio $\Upsilon_{\text{I,tot}}^{\text{ein}}$ using the Einstein mass M_{ein} . R_{ein} and M_{ein} are given in Table 5.

Total I-band luminosity within R_{ein} $L_{\text{I,ein}}$ [$10^{10} L_{\odot}$]	Mass-to-light ratio within R_{ein} $\Upsilon_{\text{I,tot}}^{\text{ein}} = M_{\text{ein}}/L_{\text{I,ein}}$ [$\Upsilon_{\text{I},\odot}$]
1.40	5.56

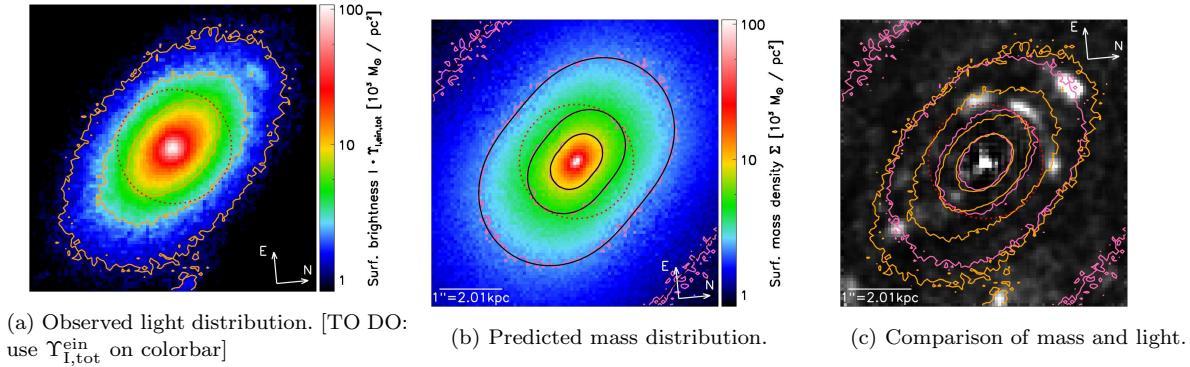


Figure 5. Comparison of the observed F814W/I-band surface brightness distribution (Panel (a) and orange contours) and predicted mass distribution from lensing constraints (Panel (b) and pink contours). To allow for a qualitative comparison of the contours in Panel (c), the light distribution was turned into a mass distribution by multiplication with the total mass-to-light ratio inside the Einstein radius $\Upsilon_{I,\text{tot}}^{\text{ein}}$ in Table 6. The Einstein radius is overplotted as red dotted circle. The uncertainties in the mass model in the second column of Table 5 were translated into random Monte Carlo noise in the mass contours. The smooth black contours correspond to the best fit model in the first column of Table 5. The background in Panel (c) shows again the surface brightness subtracted center of the galaxy to make the lensing images visible.

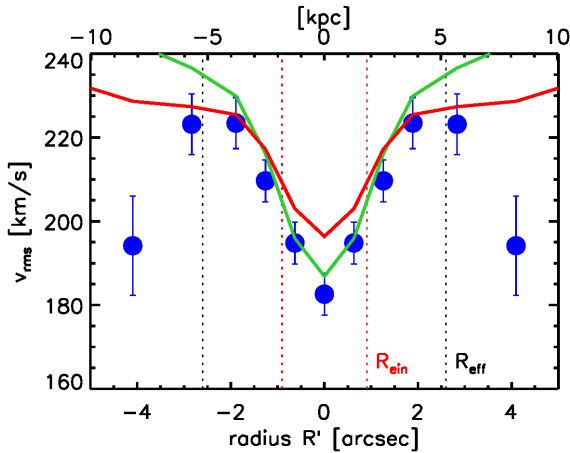


Figure 6. Comparison (not a fit!) of the symmetrized stellar v_{rms} data of J1331 (blue dots) with JAM models generated from mass distributions which were independently derived from lensing constraints in §4.2. The red solid line corresponds to the lens model for a flat rotation curve ($\alpha = 1$) in Table 5; the green line is a best fit lens model found analogously from the image positions, but for a fixed rotation curve slope of $\alpha = 1.1$. For the JAM modelling a best fit MGE to the lens mass models were used, as well as the observed surface brightness MGE in Table 2, assuming velocity isotropy $\beta_z = 0$ and an inclination of $i = 70^\circ$. The red and black dotted lines are the Einstein radius and the effective half-light radius, respectively.

modelling (e.g. van de Ven et al. (2010); Cappellari et al. (2006)), where the mass distribution is generated by multiplying the light distribution in Table 2 by a constant total mass-to-light ratio $\Upsilon_{I,\text{tot}}^{\text{dyn}}$. This assumes that the dark matter is always a constant fraction of the total matter distribution everywhere. This simplified model sometimes gives good representations of the inner parts of galaxies, where the stellar component dominates. Testing this model for J1331 is also motivated by our findings from lensing

in Section 4.2, where around the Einstein radius total and luminous mass seem to have a similar distribution.

In addition to the free fit parameter $\Upsilon_{I,\text{tot}}^{\text{dyn}}$, we also allow for a overall constant but non-zero velocity anisotropy β_z . The best fit is found by minimizing χ^2 between the v_{rms} data and model prediction and is demonstrated in Figure 7. For β_z we impose the fitting limits $\beta_z \in [-0.5, +0.5]$. While the outer parts of galaxies often show radially biased velocity anisotropy up to ~ 0.5 (from dynamical modelling of observed elliptical galaxies (e.g. Kronawitter et al. (2000)) and cosmological simulations (e.g. Diemand et al. (2004); Fukushige & Makino (2001))), the centers of galaxies are near-isotropic or have negative velocity anisotropy (Gebhardt et al. 2003). Only in extreme models (e.g. around in-spiralling supermassive black holes (Quinlan & Hernquist 1997)) velocity anisotropies as low as ~ -1 have been found. A lower limit of $\beta_z \geq -0.5$ is a realistic assumption for J1331, for which we do not expect extreme dynamical conditions. The best fit in Figure 7 however strives to very negative velocity anisotropies to be able to get the deep central dip in the v_{rms} curve. But $\beta_z = -0.5$ is not even a remotely agreeable fit and lower anisotropies are not to be expected and realistic. We also tested radial profiles for $\beta_z(R)$ of the form proposed by Baes & van Hese (2007), which was however equally unable to reproduce the data. We conclude, that this is due to the well-known degeneracy between anisotropy and mass profile [TO DO: REF] and the mass-follows-light model is *not* a good representation of the mass distribution in J1331's inner regions.

... with Increasing Mass-to-Light Ratio. In §4.2 we found from the lensing, that the light distribution might drop faster with radius than the mass distribution. This would correspond to a radially increasing total mass-to-light ratio. As velocity anisotropy alone cannot explain the observed kinematics in a simple a mass-follows-light model, we now allow for an mass-to-light ratio gradient in the JAM modelling to generate a mass model from the light distri-

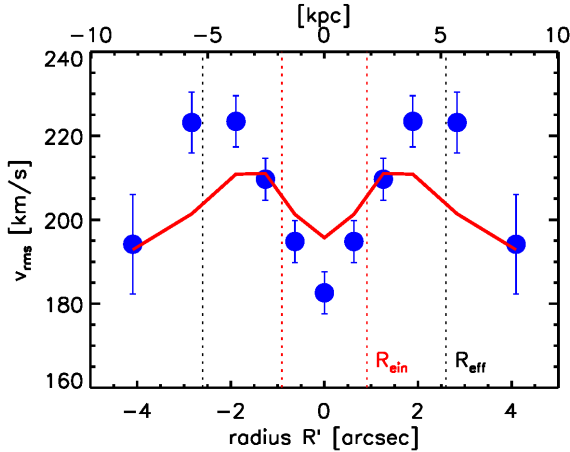


Figure 7. Comparison of the symmetrized v_{rms} data of J1331 (blue dots) with a best fit dynamical JAM model (solid red line) assuming mass-follows-light and with two free parameters: $\Upsilon_{I,\text{tot}}^{\text{dyn}}$, the total I-band mass-to-light ratio found from dynamics, which converts the observed surface brightness in Table 2 into a mass distribution, and the velocity anisotropy parameter β_z . The "best" fit is $\Upsilon_{I,*}^{\text{dyn}} = 4.8 \pm 0.1$ and $\beta_z = -0.5$, where the latter is however pegged at the lower limit of the allowed value range. This is obviously not a good model.

bution in Table 2. We do this by assigning each of the five Gaussians in the MGE its own mass-to-light ratio and replace the total luminosity in Eq. (2) L_i with the Gaussians total Mass $M_i = \Upsilon_i L_i$. We treat the five Υ_i as free parameters and only require that $\Upsilon_j \geq \Upsilon_i$ when the corresponding $\sigma_j \geq \sigma_i$ to ensure an overall mass-to-light ratio that is increasing with radius.

Figure 8b shows the (local projected) mass-to-light ratio gradient generated by the best fit to the dynamics data, which rises from $\Upsilon_{\text{tot}} = 2.53$ in the center and approaches a value of Υ_{tot} outside of the fitted region at $R' \gtrsim 3$ arcsec of $\Upsilon_{\text{tot}} = 7.60$). The central mass-to-light ratio corresponds to the Chabrier IMF stellar mass-to-light ratio found by [TO DO: REF: TREU ET AL 2011] $\Upsilon_{i,*}^{\text{Chab}} = 2.5 \pm 0.6$ [TO DO: introduce and explain????]. The strong rise of $\Upsilon_{\text{tot}}(R')$ cannot be explained by an increase in the stellar Υ_* alone [TO DO: Really??? Maybe it would have dropped again in the blue disk, if I had allowed for it????], so we deduce that we might need contribution of dark matter halo in J1331.

Fig. 8a shows that the best fit model greatly reproduces the central dip in the v_{rms} curve, even though it has slight problems fitting the drop around $R' \sim 4$ arcsec. The latter might be because we only allowed the $\Upsilon_{\text{tot}}(R')$ to rise. A slight drop could be expected when the reddish bulge turns into the bluish disk and the contribution of the stellar component becomes less due to a lower Υ_* for younger and bluer populations.

In Fig. 8b we overplot the enclosed mass profile with the Einstein mass $M_{\text{ein}} = (7.77 \pm 0.33) \cdot 10^{10} M_{\odot}$ at the Einstein radius found from lensing in Table [TO DO: REF]. The agreement between the Einstein mass and the independently found $M(< R_{\text{ein}}) = 7.49 \cdot 10^{10} M_{\odot}$ from dynamical modelling is striking.

4.4 JAM with a NFW Dark Matter Halo

Including a NFW halo. The dynamical modelling attempts in the previous sections suggest that J1331's inner regions have a slightly more roundish and at large radii more massive mass distribution than expected from the distribution of stars alone. A dark matter halo in addition to the stellar component could explain these findings. We therefore proceed by modelling the mass distribution with a) a stellar component, which we get from the light MGE in Table 2 times a constant stellar mass-to-light ratio Υ_* , and b) a spherical NFW dark matter component (Navarro et al. 1995, 1996). In the JAM modelling we use a 10-Gaussian MGE fit to the classical NFW profile

$$\rho_{\text{NFW}}(r) \propto 1/\frac{r}{R_{s,\text{NFW}}} \left(1 + \frac{r}{R_{s,\text{NFW}}}\right)^2.$$

The NFW halo has two free parameters, the scale length $R_{s,\text{NFW}}$ and a parameter describing the total mass of the halo. We use v_{200} , which is the circular velocity at the radius r_{200} within which the mean density of the halo is 200 times the cosmological [TO DO: how to express this] critical density, i.e.

$$\begin{aligned} M_{200} &= M(< r_{200}) \\ \frac{M_{200}}{\frac{4}{3}\pi r_{200}^3} &= 200\rho_{\text{crit}}(z=0) \\ v_{200} &= \sqrt{\frac{GM_{200}}{r_{200}}} \end{aligned}$$

with $\rho_{\text{crit}}(z=0) = 1.43 \cdot 10^{-7} M_{\odot}/\text{pc}^3$ in the WMAP5 cosmology by Dunkley et al. (2009). How much the mass is concentrated in the center of the NFW halo is given by the concentration of the NFW halo defined by $c_{200} \equiv r_{200}/R_{s,\text{NFW}}$. [TO DO: so toll ist das mit der Radiusbenennung noch nicht.????]. There is a close relation between the concentration and halo mass in simulations (Navarro et al. 1996). Macciò et al. (2008) found this relation for the WMAP5 cosmology (Dunkley et al. 2009) to be

$$\langle \log c_{200} \rangle (M_{200}) = 0.830 - 0.098 \log \left(h \frac{M_{200}}{10^{12} M_{\odot}} \right) \quad (21)$$

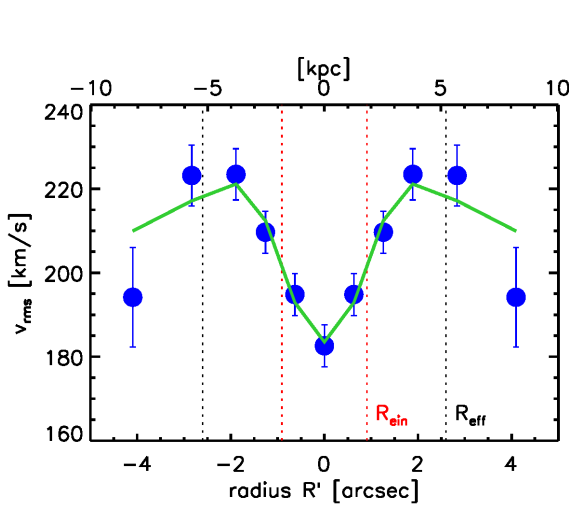
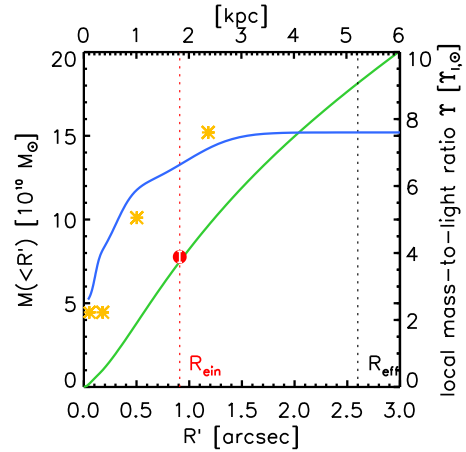
(their equation 10), with a Gaussian scatter of $\sigma_{\log c_{200}} = 0.105$ (their table A2).

Modelling. The full set of fit parameters is $(\Upsilon_{I,*}, R_{s,\text{NFW}}, v_{200}, \beta)$ [TO DO: β or β_0 ???] [TO DO: Einheitlich $\Upsilon_{I,*}$????], where β is the constant velocity anisotropy parameter (see §2.3). We will investigate this parameter space with a MCMC (Foreman-Mackey et al. 2013) and use priors for the halo parameters to guide the fit to a realistic NFW halo shape.

Dutton et al. (2010) give a relation for halo vs. stellar mass for late-type galaxies. For an Chabrier IMF stellar population they found

$$y = y_0 \left(\frac{x}{x_0} \right)^{\alpha} \left[\frac{1}{2} + \frac{1}{2} \left(\frac{x}{x_0} \right)^{\gamma} \right]^{(\beta-\alpha)/\gamma},$$

where $x = m_* [M_{\odot} h^{-2}]$ is the stellar mass, $y = \frac{\langle M_{200} \rangle}{m_*}$ and $\langle M_{200} \rangle [M_{\odot} h^{-2}]$ is the mean halo mass. The parameters for the mean and 2σ error curves for this relation are $\alpha = -0.5 \pm 0.15$, $\beta = 0$, $\gamma = 1.0$, $\log_{10} x_0 = 10.4$, $\log_{10} y_0 = -0.28^{+0.28}_{-0.24}$

(a) Comparison of v_{rms} data and best fit model.

(b) Enclosed mass and mass-to-light ratio profile. [TO DO: Make figure wider. Include legend.???] [TO DO: weird ticks on right axis???] [TO DO: Why does this plot look different than the others???] [TO DO: Switch the two y-axes. It's better to have ML on the left side, to read up the central ML.]

Figure 8. JAM model found by fitting an increasing total mass-to-light ratio Υ_{tot} profile used to generate a mass model from the light distribution. This is done by assigning a different mass-to-light ratio to each Gaussian in the MGE in Table 2. *Panel (a)*: Comparison between the stellar v_{rms} data (blue points) and the best fit model (green line). *Panel (b)*: Enclosed mass inside the projected radius R' on the sky (green line, left axis) and mass-to-light profile $\Upsilon(R')$ along the major axis [TO DO: CHECK???] (blue line, right axis) of the best fit model. The enclosed mass curve is overplotted with the independent finding for the Einstein mass $\pm 4\%$ in Table [TO DO: TABLE REFERENCE???] (red dot) at the Einstein radius (red dotted line). The best fit mass-to-light ratios of the first four Gaussians are plotted against each Gaussian σ (yellow stars). The two Gaussians with the largest σ (the fifth is not shown) have the same best fit mass-to-light ratio. Overplotted is also the effective half-light ratio R_{eff} (black dotted line).

Dutton et al. (2010). Using the stellar mass estimate for J1331 from Treu et al. (2011) $m_* = (1.06 \pm 0.25) \cdot 10^{11} M_{\odot}$ for the Chabrier IMF estimate [TO DO: introduce somewhere], we find $v_{200} = (202^{+44}_{-33})^{+12}_{-13}$. The first of the two quoted errors is due to the 2σ scatter in the relation by Dutton et al. (2010). The second error is the propagated error due to the uncertainty in the stellar mass. We use this as a rough estimate for the halo of J1331 and as Gaussian prior on v_{200} ,

$$p(v_{200}) = \mathcal{N}(200 \text{ km/s}, 40 \text{ km/s}).$$

We also use the concentration vs. halo mass relation by Macciò et al. (2008) in Eq. (21) as a prior on the concentration, i.e.

$$p(\log c_{200} | v_{200}) = \mathcal{N}(\langle \log c_{200} \rangle(M_{200}) | 0.105).$$

For the velocity anisotropy parameter β we will again employ a uniform prior

$$p(\beta) = \mathcal{U}(-0.5, +0.5)$$

to exclude very unrealistic anisotropies. The full prior used is then

$$p(\Upsilon_{I,*}, R_{S,\text{NFW}}, v_{200}, \beta) = \frac{1}{\ln(10R_{S,\text{NFW}})} p(\log c_{200} | v_{200}) \cdot p(v_{200}) \cdot p(\beta),$$

where the factor $1/\ln(10R_{S,\text{NFW}})$ is the Jacobian of the transformation from the halo parameters $(v_{200}, \log c_{200})$ [TO DO: introduce concentration] to $(v_{200}, R_{S,\text{NFW}})$.

We restrict the v_{rms} fit to a region $R' \lesssim 3.5$ arcsec, approximately within the effective half-light radius $R_{\text{eff}} = 2.6$ arcsec [TO DO: make sure R' everywhere ???]. We also include the

Einstein mass $M(< R_{\text{ein}})$ with a 10% error as an additional constraint in the fit.

Result. Figure 9 shows the posterior probability distribution of the fit sampled with an MCMC. Overplotted are also the priors used to constrain the NFW halo. The best fit parameters are summarized in Table 7. We find that the best fit NFW halo strives to be more massive and with a higher concentration than proposed by the prior. At the same time the model prefers again very negative velocity anisotropies; the sample with the highest probability is pegged at the lower limit of the prior. Both, the concentrated halo and the low anisotropy are needed to reproduce the central dip of the v_{rms} curve. [TO DO: Rewrite. Not very good.]

The first panel in Figure 11 shows the mean best fit values from Table 7.

We also fitted a model with a cored logarithmic dark matter halo. The cored halo models are in general slightly less massive than the NFW halo and therefore fit the outer regions of J1331 better. However, the density profile of the cored halo as well as the I-band light distribution within the plane drop as $\rho(r) \propto r^{-2}$, there is a strong degeneracy between the stellar mass and the dark matter. Overall we were not able to give tight constraints on the cored logarithmic halo.

Rotation curve. Following the procedure in §2.3 we find the rotation curve from the best fit mean model in Table 7 by fitting the rotation parameter κ' to the symmetrized v_{rot} data within $R' = 3.5$ arcsec. The best fit with $\kappa' = 0.76$ is shown in the second panel of Figure 11. The

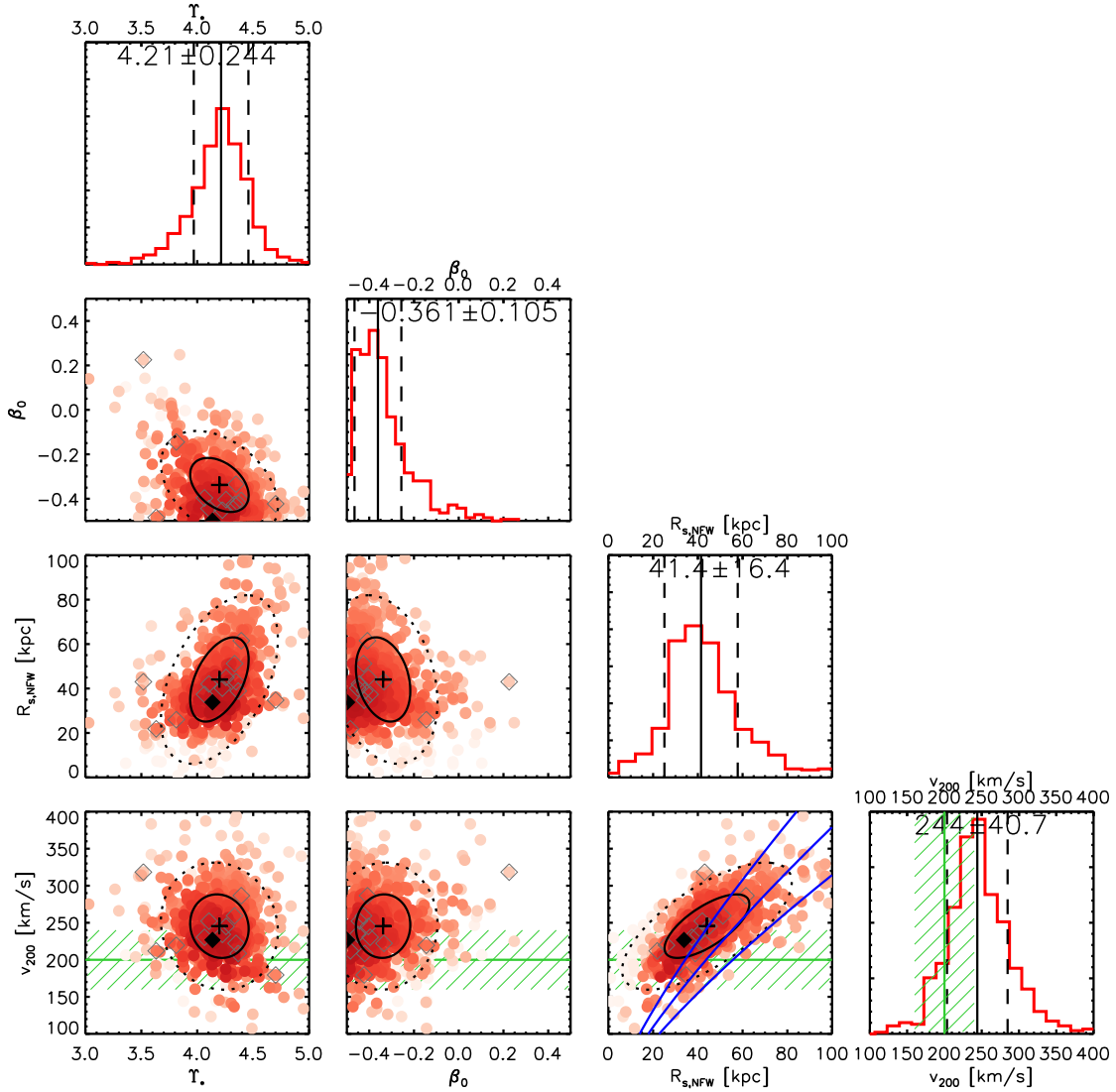


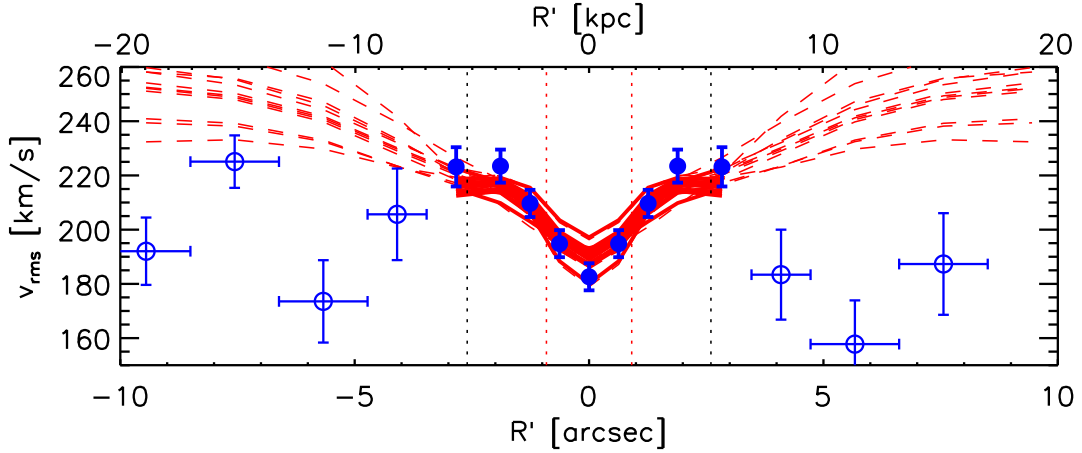
Figure 9. Posterior probability distribution sampled with MCMC (red dots and histograms) for a JAM model with NFW halo, parametrized by $R_{s,NFW}$ and v_{200} , a stellar mass distribution generated from the I-band MGE in Table 2 and a constant stellar mass-to-light ratio $\Upsilon_{I,*}$, and constant velocity anisotropy β_z . Shown are also the priors used for J1331's NFW halo, $\mathcal{N}(200\text{km/s}, 40\text{km/s})$ (green) and the concentration vs. halo mass relation by Macciò et al. (2008) from Eq. (21) in terms of v_{200} vs. $R_{s,NFW}$ with 1σ scatter (blue). The MCMC samples are color coded according to their probability (darker red for higher probability); the sample point with the highest probability is marked by a black diamond. The black cross is the mean of the distribution and the ellipses are derived from the covariance of matrix of the sample set and correspond approximately to 1σ (black solid ellipse) and 2σ (black dotted ellipse). The histograms of the marginalized 1D distributions are overplotted by the mean (black solid lines) and 1σ error (black dashed lines), whose values are also quoted in the figure and in Table 7. The grey diamonds mark a random sub-selection of 12 samples; the corresponding models are shown in Figure 10.

third panel gives the dispersion that was calculated simply by $\sigma = \sqrt{v_{rms}^2 - v_{rot}^2}$. Our assumptions for $\kappa(R)$ nicely reproduce a v_{rot} model with counter-rotating core. Although we fitted v_{rot} only to the inner regions, the extrapolation to large radii fits the data also very well. While the dispersion σ in the center fits by construction quite good, there is a huge discrepancy at large radii. The predicted dispersion is much larger than the data; we would expect the disk rotationally supported and therefore have a low velocity dispersion; es-

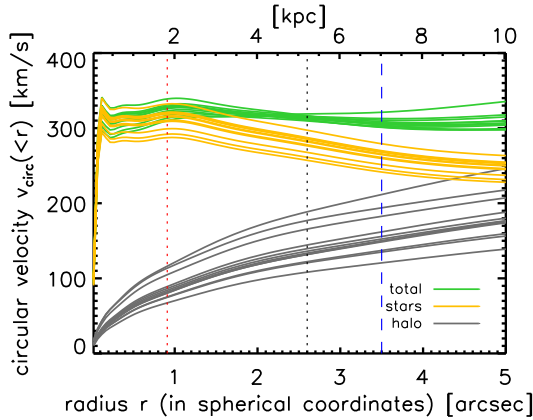
pecially dispersions as high as $\sim 200\text{km/s}$ are more likely to be observed in the pressure supported bulges of galaxies. There *might* be something unexpected with the σ measurements around ~ 5 arcsec, but at large radii the the best fit model NFW halo is simply too massive.

stellar I-band mass-to-light ratio	$\Upsilon_{I,*}$	4.2	\pm	0.2
velocity anisotropy	β_z	-0.4	\pm	0.1
NFW halo scale length	$R_{s,\text{NFW}}$ [kpc]	40	\pm	20
NFW halo virial velocity	v_{200} [km/s]	240	\pm	40
NFW halo concentration	c_{200}	8	\pm	2
NFW halo mass	M_{200} [$10^{12} M_\odot$]	5	\pm	2

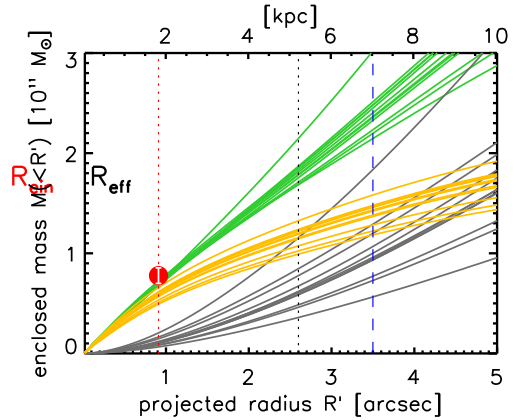
Table 7. Summary of the best fit parameters of the JAM model with NFW halo from the MCMC exploration in Figure 9. The halo mass and concentration are calculated from the the best fit $R_{s,\text{NFW}}$ and v_{200} .



(a) Comparison of the v_{rms} data with the best fit JAM models.



(b) Circular velocity curve.



(c) Enclosed mass profile.

Figure 10. Best fit JAM model including a NFW halo and velocity anisotropy with parameters given in Table 7. The 12 lines shown correspond to the 12 models randomly drawn from the posterior probability distribution and marked as grey diamonds in Figure 9. Overplotted are the Einstein radius (red dotted line) and the effective half-light radius (black dotted line). The blue dashed line marks the radius within which the data and model were fitted. *Panel a)* shows the comparison of the symmetrized v_{rms} data (solid blue points) with the best fit JAM models including a NFW halo (red solid lines). Also shown is the non-symmetrized data at larger radii (open blue dots) and an extrapolation of the best fit models, using the same model parameters but the I-band surface brightness MGE for the outer regions of J1331 derived from the Ellipse model (red dashed lines). *Panel b)* shows the circular velocity curve of the total mass (green), and separately the contribution of the stellar mass (yellow, again generated from the MGE in Table ??) and dark matter (grey). *Panel c)* shows the corresponding enclosed mass profile. Overplotted is also the Einstein mass at the Einstein radius with a 10% error, which was used in the fit as an additional constraint. [TO DO: radius benennungen sind irgendwie verrutscht]

5 DISCUSSION AND CONCLUSION

We've presented different dynamical models of the central region of J1331, some of them capturing the observed kinematics well, but none of them work both at small and large radii. In the following we will discuss possible reasons for

these deviations by also comparing our results to previous work.

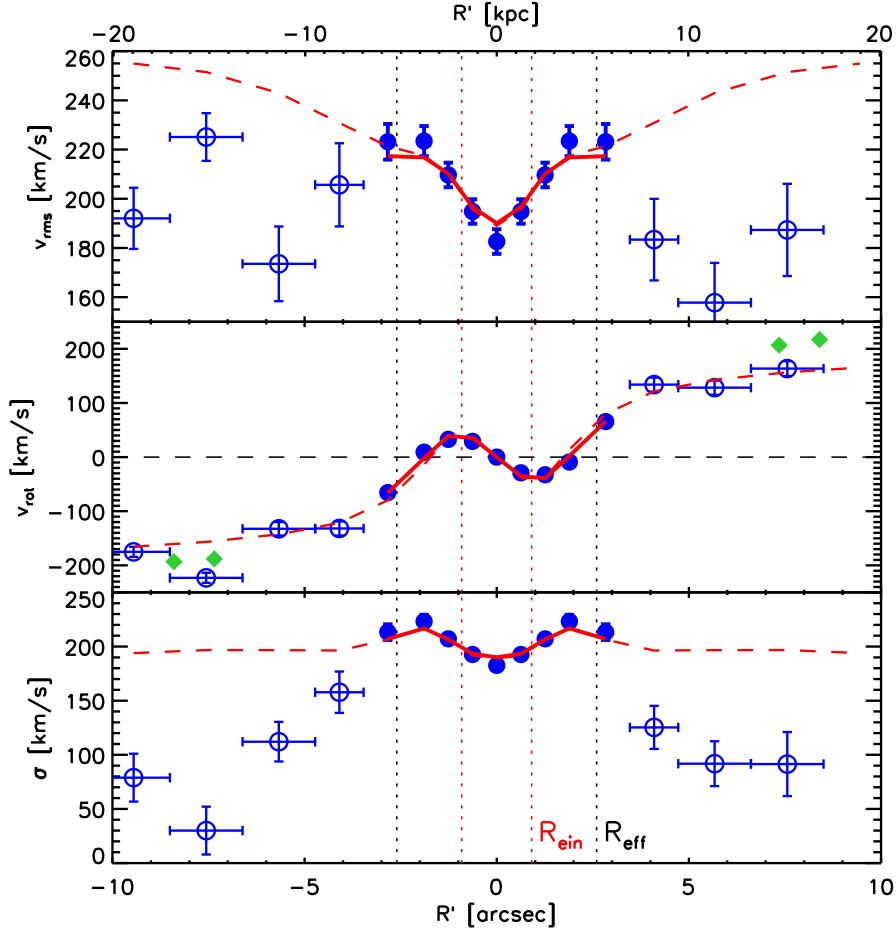


Figure 11. Generating the rotation curve from the JAM model with NFW halo and constant velocity anisotropy with the mean parameters in Table 7 and with the best fit rotation parameter $\kappa' = 0.76$ in Eq. (19) (red solid lines). The second velocity moment in the first panel and the first velocity moment in the second panel with the additional fit parameter κ' were fitted to the symmetrized data (solid blue points). The velocity dispersion is simply $\sigma = \sqrt{v_{\text{rms}}^2 - v_{\text{rot}}^2}$. At larger radii we compare the unsymmetrized data (open blue dots), the gas kinematics from Dutton et al. (2013) (green diamonds) and a JAM model using the same model parameters but the light distribution MGE generated from the Ellipse model in Figure [TO DO: REF FIGURE] as a prediction for the outer regions of J1331 (red dashed lines). The central regions are very well reproduced and we can also greatly predict the rotation curve at larger radii. Only at larger radii the v_{rms} and v_{rot} overestimate the measurements, probably due to a too massive NFW halo.

5.1 On J1331's Stellar Mass-to-Light Ratio

Further knowledge of the stellar populations within J1331 and their initial mass functions (IMF) would be useful. In particular a sophisticated guess for the *stellar* mass-to-light ratio in J1331's bulge could be compared to our very reliable measurement of the *total* mass-to-light ratio inside the Einstein radius (see Table 6) to support or contradict the presence of a lot of dark matter in the bulge.

Traditional choices for the IMF are the bottom-heavy IMF by Salpeter (1955),

$$\xi(m) \propto m^{-x}, x = 2.35,$$

(where $\xi(m)dm$ is the number of stars with mass m in $[m, m + dm]$) and the IMFs by Kroupa (2002) and Chabrier (2003), which are in agreement with each other and predict less low-mass stars.

central stellar velocity dispersion σ_0 in early-type galaxies and the IMF slope. A higher σ_0 suggests a more bottom-heavy IMF. For an unimodal (Salpeter-like) IMF and a $\sigma_0 \propto 200$ km/s for J1331 (see Figure 1d) they predict $x \approx 2.33$ (see Figure 4 in Ferreras et al. (2013)), which is close to the standard Salpeter slope. These findings are supported by Spiniello et al. (2014), who found for SDSS galaxies also a relation between unimodal (single power-law) IMF slope and stellar velocity dispersion. Their Table 2 lists $x(\sigma_* = 190 \pm 20 \text{ km s}^{-1}) = 2.08 \pm 2.08$ and $x(\sigma_* = 230 \pm 20 \text{ km s}^{-1}) = 2.33 \pm 0.4$. When assuming a bi-modal (Kroupa-equivalent-like) IMF, Ferreras et al. (2013) predict $x \approx 2.85$ (see Figure 4 in Ferreras et al. (2013)) for J1331's central velocity dispersion. This is more bottom-heavy than the standard Kroupa (2002) IMF. Overall the central velocity dispersion suggests a rather bottom-heavy IMF J1331's bulge and therefore large stellar mass-to-light ratio.

Ferreras et al. (2013) found a relation between the

Treu et al. (2011) estimated J1331's stellar bulge mass given a Salpeter IMF and measured the I-band AB magnitude of the bulge. Transformed to a stellar I-band mass-to-light ratio (see Table 8) this would correspond to $\Upsilon_{I,*}^{\text{Salpeter}} = 4.7 \pm 1.2$.

We compare our findings of the stellar mass-to-light ratios with the study by Dutton et al. (2013): Dutton et al. (2013) found that the bulge of J1331 has an IMF more bottom-heavy than the Salpeter IMF from fitting a NFW halo to (1) the Einstein mass and (2) gas kinematics at larger radii $\gtrsim 8$ arcsec. In Section 4.4 we fitted the stellar kinematics within ~ 3.5 arcsec and the Einstein mass with a NFW halo and the best fit $\Upsilon_{I,*}^{\text{dyn}} = 4.2 \pm 0.2$ (see Table 7) indicates a less bottom-heavy IMF than the Salpeter IMF. Dutton et al. (2013) found systematically lower NFW halos ($v_{\text{circ}}(5\text{arcsec}) \sim 120\text{km s}^{-1}$ according to their Figure 2) than we did ($v_{\text{circ}}(5\text{arcsec}) \sim 200\text{km s}^{-1}$, see Figure 1d). We note however, that our results would be much closer to those by Dutton et al. (2013), if we only used the lensing results at small radii as they did: The total mass-to-light ratio of $\Upsilon_{I,\text{tot}}^{\text{ein}} = 5.6$ inside the Einstein radius (see Table 6). In case of a lower mass dark matter halo, the largest contribution to this mass-to-light ratio would then be stellar mass. And the corresponding IMF would be more bottom-heavy than Salpeter, like what Dutton et al. (2013) found. The circular velocity curve $v_{\text{circ}}(R) = \sqrt{R \frac{\partial \Phi}{\partial R}}|_{z=0}$ Dutton et al. (2013) find for J1331 peaks at $v_{\text{circ}}(R \sim 0.9\text{arcsec}) \sim 350\text{km s}^{-1}$ (from lensing constraints only) and at $v_{\text{circ}}(R \sim 0.9\text{arcsec}) \sim 370\text{km s}^{-1}$ (when including a dark matter halo and gas kinematics in the fit). We get a very similar circular velocity curve (at least at small radii) for a mass-follows-light model with constant $\Upsilon_{I,\text{tot}}^{\text{ein}} = 5.6$, which peaks at $v_{\text{circ}}(R \sim 0.9\text{arcsec}) \sim 360\text{km s}^{-1}$. From this comparison follows, that the model by ? corresponds approximately to a mass-follows-light model in the inner regions of J1331. In Section 4.3 however we showed, that this is *not* a good model for J1331 and won't be able to reproduce the central stellar v_{rms} dip. On the other hand, because our NFW JAM models fail to predict the stellar kinematics at large radii, the true halo parameters are more likely closer to the findings by Dutton et al. (2013).

All of this leaves the central dip unexplained: It cannot be due to tangential velocity anisotropy in the center alone (see Section 4.3, Figure 7). It also cannot be explained by a strong contribution of dark matter inside the bulge together with a moderate tangential velocity anisotropy, because the corresponding dark matter halos would still be too massive to fit the data in the outer regions (see Section 4.4, Figure 10a)).

An alternative JAM model was introduced in Section 4.3, where we used the surface brightness distribution without a halo component but together with an increasing mass-to-light ratio. We found that such a model would be perfectly consistent with the lensing results and predict a total mass-to-light ratio in the center of J1331 of $\Upsilon_{I,\text{tot}}(R \sim 0) = 2.53$. This is very close to the stellar mass-to-light ratio we got from Treu et al. (2011) estimates of the bulge's stellar mass using the Chabrier IMF $\Upsilon_{I,*}^{\text{Chabrier}} = 2.5 \pm 0.6$, i.e. less bottom-heavy (more bluish)

population.

The above discussion motivates the following speculation: In the absence of a strong dark matter contribution in the center, the overall stellar-mass-to-light ratio within the Einstein radius indicates a bottom-heavy IMF close to the Salpeter IMF, consistent with estimates from the velocity dispersion. At the same time the central dip can then be only explained, if there was an increase in stellar mass-to-light ratio with radius *within* the bulge. *If* there was a central stellar population with an IMF close to the Chabrier (2003) IMF, surrounded by a more bottom-heavy population, the central stellar kinematics would be well explained and be fully consistent with the lensing results. (According to Figure 5c the lensing result might not predict a mass to light ratio gradient inside R_{ein} , but then again the mass slope $\alpha = 1$ was only weakly constrained.) It is not expected that the bluish disk of J1331 has a $\Upsilon_{I,*}$ as high as the reddish bulge. The kinematics at larger radii would then also be much better recovered by lower mass dark matter halo as found by Dutton et al. (2013).

Standard JAM modelling approaches seem not to work for J1331. A JAM model for J1331 would need to allow for stellar mass-to-light ratio gradients within the galaxy, velocity anisotropy and a dark matter halo. Because of degeneracies between stellar and dark mass, and matter distribution and anisotropy profile, such a dynamical model would not lead to very tight constraints on the model parameters. Further priors are needed. Detailed stellar population analyses of the spectra taken along J1331's major axis could possibly support or contradict the suspicion of the existence of stellar mass-to-light ratio gradients in J1331.

[TO DO: Rewrite the paper such, that it's main message is, that there is a strong indication of increasing stellar mass-to-light ratio in the center of the galaxy, i.e. a bluish core, because neither velocity anisotropy, neither a strong dark matter contribution alone can explain all dynamical signatures. "Evidence from Lensing and Dynamics for a bluish core in the center of J1331" as a possible alternative title??? Eher nicht...]

[TO DO: Einheitlich: $\Upsilon_{I,*}^{\text{comment}}$, $\Upsilon_{I,\text{tot}}^{\text{ein}}$]

5.2 Does J1331 have a Merger History?

[TO DO]

5.3 Summary

[TO DO]

REFERENCES

- Baes M., van Hese E., 2007, *Astronomy and Astrophysics*, 471, 419
- Barnabè M., Dutton A. A., Marshall P. J., Auger M. W., Brewer B. J., Treu T., Bolton A. S., Koo D. C., Koopmans L. V. E., 2012, *Monthly Notices of the RAS*, 423, 1073
- Bendinelli O., 1991, *Astrophysical Journal*, 366, 599
- Binney J., Merrifield M., 1998, *Galactic Astronomy*

	L [$10^{10} L_{\odot}$]	Chabrier IMF		Salpeter IMF	
		M_* [$10^{10} M_{\odot}$]	$\Upsilon_{I,*}^{\text{chab}}$	M_* [$10^{10} M_{\odot}$]	$\Upsilon_{I,*}^{\text{Salpeter}}$
bulge	3.10 ± 0.15	7.8 ± 1.8	2.5 ± 0.6	14.5 ± 3.7	4.7 ± 1.2
disk	2.35 ± 0.11	2.9 ± 0.7	1.2 ± 0.3	5.2 ± 1.1	2.2 ± 0.5
total	5.45 ± 0.19	10.6 ± 1.9		19.7 ± 3.9	

Table 8. Total I-band luminosity, stellar mass and mass-to-light ratio, calculated from the I-band AB magnitudes and stellar masses found for J133's bulge and disk by ? (their table 2) for comparison with this work. The transformation from AB magnitudes to the Johnson-Cousins I-Band used the relation $I[\text{mag}] = I[\text{ABmag}] - 0.309$ from Frei & Gunn (1994) (their table 2). For the conversion from apparent magnitude to total luminosity the redshift $z = 0.113$ Brewer et al. (2012) was turned into a luminosity distance using the cosmology by ??.

Brewer B. J., Dutton A. A., Treu T., Auger M. W., Marshall P. J., Barnabè M., Bolton A. S., Koo D. C., Koopmans L. V. E., 2012, *Monthly Notices of the RAS*, 422, 3574

Brewer B. J., Marshall P. J., Auger M. W., Treu T., Dutton A. A., Barnabè M., 2014, *Monthly Notices of the RAS*, 437, 1950

Cappellari M., 2002, *Monthly Notices of the RAS*, 333, 400

Cappellari M., 2008, *Monthly Notices of the RAS*, 390, 71

Cappellari M., Bacon R., Bureau M., Damen M. C., Davies R. L., de Zeeuw P. T., Emsellem E., Falcón-Barroso J., Krajnović D., Kuntschner H., McDermid R. M., Peletier R. F., Sarzi M., van den Bosch R. C. E., van de Ven G., 2006, *Monthly Notices of the RAS*, 366, 1126

Chabrier G., 2003, *Publications of the ASP*, 115, 763

Diemand J., Moore B., Stadel J., 2004, *Monthly Notices of the RAS*, 352, 535

Dolphin A. E., 2000, *Publications of the ASP*, 112, 1397

Dolphin A. E., , 2008, *Zero Points relative to Holtzman et al.* (1995)

Dunkley J., Komatsu E., Nolte M. R., Spergel D. N., Larson D., Hinshaw G., Page L., Bennett C. L., Gold B., Jarosik N., Weiland J. L., Halpern M., Hill R. S., Kogut A., Limon M., Meyer S. S., Tucker G. S., Wollack E., Wright E. L., 2009, *Astrophysical Journal, Supplement*, 180, 306

Dutton A. A., Brewer B. J., Marshall P. J., Auger M. W., Treu T., Koo D. C., Bolton A. S., Holden B. P., Koopmans L. V. E., 2011, *Monthly Notices of the RAS*, 417, 1621

Dutton A. A., Conroy C., van den Bosch F. C., Prada F., More S., 2010, *Monthly Notices of the RAS*, 407, 2

Dutton A. A., Treu T., Brewer B. J., Marshall P. J., Auger M. W., Barnabè M., Koo D. C., Bolton A. S., Koopmans L. V. E., 2013, *Monthly Notices of the RAS*, 428, 3183

Emsellem E., Dejonghe H., Bacon R., 1999, *Monthly Notices of the RAS*, 303, 495

Emsellem E., Monnet G., Bacon R., 1994, *Astronomy and Astrophysics*, 285, 723

Evans N. W., Witt H. J., 2003, *Monthly Notices of the RAS*, 345, 1351

Ferreras I., La Barbera F., de la Rosa I. G., Vazdekis A., de Carvalho R. R., Falcón-Barroso J., Ricciardelli E., 2013, *Monthly Notices of the RAS*, 429, L15

Foreman-Mackey D., Hogg D. W., Lang D., Goodman J., 2013, *Publications of the ASP*, 125, 306

Frei Z., Gunn J. E., 1994, *Astronomical Journal*, 108, 1476

Fukushige T., Makino J., 2001, *Astrophysical Journal*, 557, 533

Gebhardt K., Richstone D., Tremaine S., Lauer T. R., Bender R., Bower G., Dressler A., Faber S. M., Filippenko A. V., Green R., Grillmair C., Ho L. C., Kormendy J., Magorrian J., Pinkney J., 2003, *Astrophysical Journal*, 583, 92

Holtzman J. A., Burrows C. J., Casertano S., Hester J. J., Trauger J. T., Watson A. M., Worthey G., 1995, *Publications of the ASP*, 107, 1065

Kochanek C. S., 1991, *Astrophysical Journal*, 373, 354

Kronawitter A., Saglia R. P., Gerhard O., Bender R., 2000, *Astronomy and Astrophysics, Supplement*, 144, 53

Kroupa P., 2002, *Science*, 295, 82

Macciò A. V., Dutton A. A., van den Bosch F. C., 2008, *Monthly Notices of the RAS*, 391, 1940

Monnet G., Bacon R., Emsellem E., 1992, *Astronomy and Astrophysics*, 253, 366

Narayan R., Bartelmann M., 1999, in Dekel A., Ostriker J., eds, *Formation of Structure in the Universe, Proceedings of the 1995 Jerusalem Winter School Lectures on Gravitational Lensing*. Cambridge University Press, pp 360–432

Navarro J. F., Frenk C. S., White S. D. M., 1995, *Monthly Notices of the RAS*, 275, 720

Navarro J. F., Frenk C. S., White S. D. M., 1996, *Astrophysical Journal*, 462, 563

Oort J. H., 1932, *Bulletin Astronomical Institute of the Netherlands*, 6, 249

Quinlan G. D., Hernquist L., 1997, *New Astronomy*, 2, 533

Rubin V. C., Thonnard N., Ford Jr. W. K., 1978, *Astrophysical Journal, Letters*, 225, L107

Salpeter E. E., 1955, *Astrophysical Journal*, 121, 161

Spiniello C., Trager S., Koopmans L. V. E., Conroy C., 2014, *Monthly Notices of the RAS*, 438, 1483

Treu T., 2010, *Annual Review of Astron and Astrophys*, 48, 87

Treu T., Dutton A. A., Auger M. W., Marshall P. J., Bolton A. S., Brewer B. J., Koo D. C., Koopmans L. V. E., 2011, *Monthly Notices of the RAS*, 417, 1601

van de Ven G., Falcón-Barroso J., McDermid R. M., Cappellari M., Miller B. W., de Zeeuw P. T., 2010, *Astrophysical Journal*, 719, 1481

van den Bosch R. C. E., van de Ven G., Verolme E. K., Cappellari M., de Zeeuw P. T., 2008, *Monthly Notices of the RAS*, 385, 647